Chapter 7

A state-insensitive, compensated nanofiber trap

In this chapter, we discuss a scheme to trap single atoms in the vicinity of a tapered optical nanofiber with minimal internal atomic state intrusions (in Sec. 7.2); the fabrication of a suitable nanofiber with certain properties required to realize such an atom trapping scheme (in Sec. 7.3); and the demonstration of single atom trapping with state insensitivity of the internal atomic state. The state insensitivity of the scheme is important for allowing long trap and coherence lifetimes, as well as in cavity QED systems (e.g., in a single nanofiber cavity system or hybrid nanofiber-microtoroid system as discussed in Chapter 6) in maintaining atomic transition frequency to be resonant to the optical cavity that may have narrow cavity linewidth.

This chapter is based on references [142] and [91]. The realization and achievements made in our experiment using this tapered nanofiber platform are a result of collaboration and work of many individuals, which I would like to acknowledge here. Firstly, I would like to acknowledge the group of Prof. Arno Rauschenbeutel of the University of Vienna for the pioneering work in optical nanofiber system, which forms the basis of our system. The work described in this chapter is a result of the team collaboration of the nine authors of the two manuscripts, whose contributions I would like to acknowledge here. Kyung Soo Choi and I contributed to the initial ideas, calculations, and trapping schemes. Kyung Soo Choi, Akihisa Goban, and Clement Lacroute contributed to the full calculations with full light-shift Hamiltonian. Kyung Soo Choi and Akihisa Goban led in carrying out our experiment, taking measurements and in data analysis. I led in the development of a new taper pulling setup, the fabrication and characterization of nanofiber and the incorporation of the nanofiber device sealed into our vacuum chamber. This is a joint experiment between Lab 2 (with contributing members Ding Ding, Martin Pototschnig) and Lab 1 (with contributing members Tobias Thiele, Clement Lacroute, Nate Stern). This work was carried out under the guidance and

supervision of my advisor, Prof. Jeff Kimble at Caltech.

7.1 Background

An exciting frontier in quantum information science is the integration of otherwise "simple" quantum elements into complex quantum networks [132]. The laboratory realization of even small quantum networks enables the exploration of physical systems that have not heretofore existed in the natural world. Within this context, there is active research to achieve lithographic quantum optical circuits, for which atoms are trapped near micro- and nanoscopic dielectric structures and "wired" together by photons propagating through the circuit elements. Single atoms and atomic ensembles endow quantum functionality for otherwise linear optical circuits and thereby the capability to build quantum networks component by component.

Creating optical traps compatible with the modal geometries of micro- and nano-scopic optical resonators and waveguides [240, 73] is a long-standing challenge in AMO physics [179, 246, 35]. 'Optical tweezers' with tight focussing have succeeded in trapping single atoms within small volumes $\sim \lambda^3$ [211], but the focal geometries of conventional optical elements are not compatible with atomic localization $\simeq 100$ nm near microscopic photonic structures [240, 73]. Moreover, spatially inhomogeneous energy shifts $U(\mathbf{r})$ on a sub-wavelength scale generally depend on the atomic internal state, limiting long-lived trap and coherence times due to single-photon scattering events with energies much larger than the recoil energy and to spatially dependent frequency shifts for the components of atomic superpositions [61, 53, 142].

7.2 Scheme and trap potential

7.2.1 Introduction

Laser trapping and interfacing of laser-cooled atoms in an optical fiber network is an important capability for quantum information science. Following the pioneering work of Balykin *et al.* and Vetsch *et al.*, here I discuss a robust method of trapping single cesium atoms with a two-color state-insensitive evanescent wave around a dielectric nanofiber. Specifically, I show that vector light shifts (i.e., effective inhomogeneous Zeeman broadening of the ground states) induced by the inherent ellipticity of the forward-propagating evanescent wave can be effectively canceled by a backward-propagating evanescent wave. Furthermore, by operating the trapping lasers at the magic

wavelengths, the differential scalar light shift between ground and excited states are removed, thereby allowing for resonant driving of the optical D_2 transition. This scheme provides a promising approach to trap and probe neutral atoms with long trap and coherence lifetimes with realistic experimental parameters.

The development of a matter-light quantum interface using cold atoms and optical fibers has been an active field of research over the past few years [132]. Recent advances towards this goal include the observation of electromagnetically induced transparency and the loading of ultracold atoms in hollow-core optical fibers [196, 113, 49, 15], as well as the trapping and probing of atomic ensembles via the evanescent fields surrounding tapered nanofibers [248, 129, 173, 206]. While prominent examples of off-resonant interaction between evanescent waves and matter have used a plane dielectric geometry for atom optics and interferometry [18, 54] as well as for surface traps of quantum degenerate gases [178, 204, 16], recent progress of atom-light interactions with optical waveguides [49, 15, 129, 173, 206] sets the stage for the fiber integration of free-space quantum systems in a quantum network via quantum-state transfer between matter and light [31, 45, 98, 208] and for strong coupling of single atoms and photons trapped near microcavities [9, 5, 228, 20, 50, 238]. Furthermore, these effective 1-dimensional systems may be applied for investigating quantum many-body phenomena in low dimensions with long-range interactions mediated by the waveguide [262, 136, 219, 42].

One major drawback of many optical traps is that spatially inhomogeneous energy shifts $U(\mathbf{r})$ generally depend on the atomic electronic state, limiting the long-lived trap and coherence times necessary for repeated coherent operations [53]. This is traditionally alleviated by constructing a *state-insensitive* optical trap designed to decouple atomic transition frequencies from the spatially varying potential of each electronic state [258]. Specifically, at the "magic" wavelength conditions, the differential response of the dynamic scalar polarizabilities $\alpha^{(0)}(\omega)$ for the ground and excited states $\alpha^{(0)}_{|g\rangle}, \alpha^{(0)}_{|e\rangle}$ at the optical frequency ω can be tailored such that both levels are perturbed identically with $\alpha^{(0)}_{|g\rangle} = \alpha^{(0)}_{|e\rangle}$. This leads to a vanishing differential atomic level shift $\delta U_{\text{scalar}} = 0$ [258, 133, 121, 112, 162]. Differential shifts for the hyperfine ground states can be minimized by using far off-resonant beams, whereas Zeeman coherence can be conveniently protected by using linearly polarized light in which the vector light shifts are zero.

Although such magic wavelengths can be used for nanofiber traps [128], the strongly guiding nature of the waveguide inevitably leads to non-negligible longitudinal electric fields $\mathbf{E}_z$ in the evanescent region, which are out of phase with the transverse field $\mathbf{E}_\perp = (\mathbf{E}_x, \mathbf{E}_y)$. Here, z refers

to the direction parallel to the fiber axis, while x and y are the coordinates perpendicular to the fiber axis. The resulting local polarization at location $\mathbf{r}$ is in general elliptical even for linearly polarized input beams, and induces vector shifts U_{vector}. The differential vector shift δU_{vector} in turn manifests itself as a "fictitious magnetic field", leading to inhomogeneous Zeeman broadening [71]. Furthermore, the spatially varying elliptical polarization of the evanescent field on a scale $\delta r < \lambda$ renders it difficult to cancel δU_{vector} using bias fields, resulting in increased heating rate [53] and limited coherence time [77].

Building upon the recent realization of a nanofiber trap as proposed in Ref. [17, 125] and demonstrated in Refs. [248, 56], our group proposed a promising strategy for a state-insensitive evanescent field trap. Differential scalar shifts δU_{scalar} between $|g\rangle$ and $|e\rangle$ are canceled using "magic" wavelength conditions. The inhomogeneous Zeeman broadening δU_{vector} caused by a forward propagating blue-detuned field $\mathbf{E}^{(\text{fwd})}$ is canceled by a backward propagating field $\mathbf{E}^{(\text{bwd})}$ with a small relative frequency detuning δ_{fb}. Thus, our scheme can compensate for the light shifts of the strongly guided evanescent waves to the first order in the space external to the dielectric fiber, leading to favorable parameters for the realization of a long-lived fiber-integrated quantum memory and resonant coupling to ultra-high quality micro-cavities based on optically trapped atoms.

7.2.2 Scheme

By appropriately combining blue-detuned and red-detuned fields $\mathbf{E}_{\text{red}}$ and $\mathbf{E}_{\text{blue}}$ guided along an optical nanofiber, an atomic trapping potential can be engineered from the evanescent electric fields [17, 125]. Briefly speaking, radial confinement can be achieved with a short wavelength blue-detuned guided field (e.g., $\lambda_{\text{blue}} = 687$ nm) that provides a short extent evanescent field repulsive potential, and a longer wavelength red-detuned guided field (e.g., $\lambda_{\text{red}} = 937$ nm) that provides an attractive potential over a longer exponential evanescent field decay length. By optimizing the power ratio between the red- and blue-detuned FORT beams and taking into account the attractive Casimir-Polder surface potential, one can create an atomic trap potential along the radial direction r with a potential well located at $r_{\text{trap}} \sim 200$ nm from the surface of the nanofiber. Recall that the exact mode profile of the fundamental nanofiber guided mode, HE_{11} can be solved analytically, as discussed in Sec. 3.2.1.1. In addition to radial confinement, one can exploit the azimuthal mode profile of the fundamental HE_{11} mode by using a linearly polarized beam, which breaks the azimuthal symmetry of the mode. The red-detuned and blue-detuned mode profiles with wavelengths 937nm and 687nm respectively are shown by the first two panel columns in the first and second row of

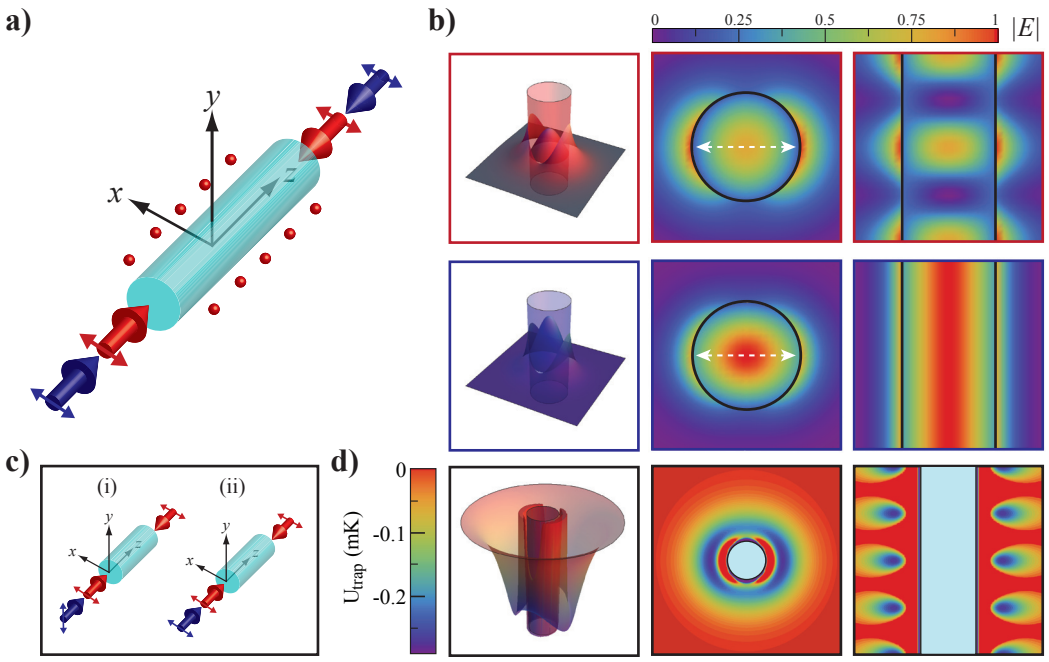

Figure 7.1: **Nanofiber atom trap scheme. a)** Schematic of our magic-compensated nanofiber trap scheme, consisting of two pairs of red- and blue-detuned counter-propagating x-polarized beams. **b)** Electric field profiles for x-polarized $\lambda_{\text{red}} = 937$ nm red-detuned (first row) and $\lambda_{\text{blue}} = 687$ nm blue-detuned (second row) beams on the $x-y$ plane (second column) and $x-z$ plane (third column), with 3D cartoon illustration in first column. **c)** Other schemes utilizing pair of red-detuned beams and a single blue-detuned beam, with orthogonal and parallel polarizations in (i) and (ii) respectively. **d)** Ground state (cesium $6S_{1/2}, F = 4$) trap potential for the scheme shown in a) with $\lambda_{\text{red}} = 937$ nm, $P_{\text{red}} = 2\times$ 0.4 mW, $\lambda_{\text{blue}} = 687$ nm, $P_{\text{blue}} = 2\times$ 5 mW, nanofiber radius $a = 215$ nm, with a simple Casimir-Polder potential $U_{\text{CP}} \sim -1/r^3$ near the surface of nanofiber.

Fig. 7.1 respectively. Thus together, the optimization process which is a function of the FORT beam wavelengths, powers, and the diameter of the nanofiber, lead to desired radial and azimuthal trapping potential. Finally, to confine atoms in three dimensions, a counter-propagating red-detuned beam can be added to form a standing-wave pattern that creates a one-dimensional lattice potential along the fiber axis. Therefore all together, a minimum number of one blue-detuned FORT beams and a pair of two counter-propagating red-detuned FORT beams are required to provide three-dimensional confinement of an atom in this scheme. We note that the polarization directions of the red-detuned and blue-detuned beams need not be the same (e.g., both can be along x-axis, or one can be along x-axis while the other is along y-axis).

In the landmark experiment of [248], a pair of red-detuned, x-polarized beams, and a single blue-detuned, y-polarized beam are used, as illustrated in Fig. 7.1 c) (i). As can be seen from the nanofiber mode profile (see Fig. 3.5 c) (i) and (iv)), this configuration has the advantage of minimizing the amount of longitudinal component of the out-of-phase electric field, E_z, at the trap

location (along the red-detuned FORT polarization direction) which as we shall discuss, leads to intrusive adverse effects due to vector shift component in the atom Stark shifts. It is important to note that although the E_z component is minimized at the trap location in this configuration, it can be non-negligible at other positions, due to the finite size of the trap potential well. We also note that, as can be seen from the mode profile, the intensity of the blue-detuned FORT is relatively small at the trap location, requiring a larger amount of blue-detuned FORT power to provide a sufficient repulsive potential.

An alternative scheme would be to use the three beams with parallel polarizations, as illustrated in Fig. 7.1 c) (ii). This scheme allows for the use of lower power for the blue-detuned beam, by about a factor of three for the parameters that we will consider in section 7.2.6, but results in larger vector shifts, as we will discuss in the next sections. The scheme that we propose in this chapter makes use of four beams with parallel linear input polarizations, as shown in Fig. 7.1 a). The additional blue-detuned beam compensates for the vector shifts of its companion blue-detuned beam, as we will discuss in the next sections. The panels in Fig. 7.1 b) show the electric field amplitude $|E|$ of the red-detuned and blue-detuned beams in the first and second row respectively, and in the third row, the resulting trap potential using the parameters for our experimental demonstration described in Sec. 7.4, $P_{\mathrm{red}} = 2 \times 0.4$ mW and $P_{\mathrm{blue}} = 2 \times 5$ mW, $\lambda_{\mathrm{red1}} = \lambda_{\mathrm{red2}} = 937.1$ nm, $\lambda_{\mathrm{blue1}} = 686.1$ nm, $\lambda_{\mathrm{blue2}} = 686.7$ nm. The first panel column shows 3D illustration of the electric field $|E|$ and potential U_{trap} while the two last columns show transverse XY- and longitudinal XZ-cross-sections (at y=0). Note that the red-detuned beam forms a standing wave pattern along the fiber axis, while the interference pattern for the counter-propagating blue-detuned beams gets averaged out, as we apply a small detuning between the two blue-detuned beams, to avoid super-lattice formation.

Summarizing our discussion so far in this section, we discuss how by appropriately combining red-detuned and blue-detuned guided FORT beams through a nanofiber, an atom trap potential can be engineered providing three-dimensional confinement of atoms. We discuss various beam configurations particularly related to the number of beams and their polarization orientations, also how they affect the extent of vector shifts in the atom Stark shift, which one would like to minimize to avoid intrusions to the trapped atom internal states. As discussed before, in general FORT beam wavelengths would produce non-uniform ac Stark shifts to the ground and excited states of the atom, leading to variations in the atomic ground to excited state transition frequency as an atom moves within a trap (or in the low energy regime, leading to a broadening of the transition frequency as an atom occupies a trapped state). The last part of our scheme, in addition to using

the two pairs of counter-propagating red- and blue-detuned beams, is to use the magic wavelengths for the FORT beams (which for cesium D2 line, are $\lambda_{\text{red}} \approx 937$ nm and $\lambda_{\text{blue}} \approx 687$ nm), which lead to equal scalar light shifts for both the ground and excited state atom levels, maintaining the transition frequency. Thus, in summary, our scheme involves red- and blue-detuned FORT beams that produce radial and azimuthal trapping potential (at magic wavelength conditions to provide differential scalar shift cancellation), a third (counter-propagating red-detuned) beam that provides longitudinal confinement, and a fourth (blue-detuned) beam slightly detuned from the other blue-detuned beam, providing approximate vector shift cancellation. In the next section, we will discuss the mathematical model we use to calculate the resulting trap potential using this scheme.

7.2.3 Light shift Hamiltonian

An atom's energy levels and corresponding eigenfunctions are perturbed in the presence of a relatively weak electric field (weak relative to the fine and hyperfine structure). Intuitively, one can envisage the presence of an electric field that modifies the charge distribution of the atom's electrons relative to its nuclei, and consequently changes the electronic state energy levels. For an oscillating electric field, such as one associated with a propagating laser beam, the perturbation in the atom's energy level is referred to as the ac Stark effect. In the subsequent discussions below, we first start with a general interaction Hamiltonian for an atom in the presence of an electric field, then proceed to formulating the equations appropriate for the above conditions, to calculate the AC Stark effects, which could lead to shifting, mixing, and splitting of atomic levels.

The interaction Hamiltonian for an atom interacting with an electric field $\mathbf{E}$, the light-shift Hamiltonian, is given in the dipole approximation by $\hat{H}_{\text{ls}} = -\hat{\mathbf{d}} \cdot \hat{\mathbf{E}}$, where $\hat{\mathbf{d}}$ is the electric dipole operator and $\hat{\mathbf{E}}$ is the electric field operator. Using Floquet perturbation theory, treating hyperfine interaction and interaction with the electric field perturbatively, this light-shift Hamiltonian can be decomposed into its Cartesian components (x, y, z) parameterized by the dynamic polarizability $\alpha(\omega)$ [202, 21, 130, 142, 64][1]:

$$\begin{aligned}\hat{H}_{\text{ls}} &= \hat{H}_0 + \hat{H}_1 + \hat{H}_2 \\ &= -\alpha^{(0)}\hat{\mathbf{E}}^{(-)} \cdot \hat{\mathbf{E}}^{(+)} - i\alpha^{(1)} \tfrac{\left(\hat{\mathbf{E}}^{(-)} \times \hat{\mathbf{E}}^{(+)}\right)\cdot \hat{\mathbf{F}}}{2F} \\ &- \sum_{\mu,\nu} \alpha^{(2)} \hat{E}_{\mu}^{(-)} \hat{E}_{\nu}^{(+)} \tfrac{3}{F(2F-1)} \left[\tfrac{1}{2}(\hat{F}_{\mu}\hat{F}_{\nu} + \hat{F}_{\nu}\hat{F}_{\mu}) - \tfrac{1}{3}\hat{F}^2\delta_{\mu\nu}\right],\end{aligned} \tag{7.1}$$

where $\alpha^{(0)}$, $\alpha^{(1)}$ and $\alpha^{(2)}$ are the scalar, vector and tensor atomic dynamic polarizabilities, $\hat{\mathbf{E}}^{(+)}$

[1] Note that there are certain errors made in [142]. See [64] for corrections.

and $\hat{\mathbf{E}}^{(-)}$ are the positive and negative frequency components of the electric field, $\hat{\mathbf{F}} = \hat{\mathbf{I}} + \hat{\mathbf{J}}$ is the atomic total angular momentum operator, with $\hat{\mathbf{I}}$ and $\hat{\mathbf{J}}$ the nuclear and electronic angular momentum operators, $\mu, \nu \in \{x, y, z\}$ are components in the Cartesian basis, and $\hat{H}_0$, $\hat{H}_1$, and $\hat{H}_2$ are the terms associated with the scalar, vector, and tensor light shifts, respectively. Note that $\alpha^{(0)}$, $\alpha^{(1)}$, and $\alpha^{(2)}$ of Eq. (7.1) include counter-rotating terms. The dynamic polarizabilities are given by [64]:

$$\alpha^{(0)}(J,F) = \sum_{nJ'F'} \frac{d_{JJ'}^2}{3}(2F'+1) \begin{Bmatrix} J & J' & 1 \\ F' & F & I \end{Bmatrix}^2 G_{FF'}^{(0)}, \tag{7.2}$$

$$\begin{aligned} \alpha^{(1)}(J,F) &= 2\sum_{nJ'F'} (-1)^{F+F'} d_{JJ'}^2 \sqrt{\frac{3F(2F+1)}{2(F+1)}} \begin{Bmatrix} 1 & 1 & 1 \\ F & F & F' \end{Bmatrix}, \\ &\quad \times (2F'+1) \begin{Bmatrix} J & J' & 1 \\ F' & F & I \end{Bmatrix}^2 G_{FF'}^{(1)} \end{aligned} \tag{7.3}$$

$$\begin{aligned} \alpha^{(2)}(J,F) &= \sum_{nJ'F'} (-1)^{F+F'} d_{JJ'}^2 \sqrt{\frac{10F(2F+1)(2F-1)}{3(F+1)(2F+3)}} \begin{Bmatrix} 1 & 1 & 2 \\ F & F & F' \end{Bmatrix}, \\ &\quad \times (2F'+1) \begin{Bmatrix} J & J' & 1 \\ F' & F & I \end{Bmatrix}^2 G_{FF'}^{(2)}, \end{aligned} \tag{7.4}$$

where $G_{ij}^{(K)}$ is the rank-K propagator defined as

$$G_{ij}^{(K)} = \frac{1}{\hbar}\left\{\frac{1}{\omega_{ji} - \omega} + \frac{(-1)^K}{\omega_{ji} + \omega}\right\}, \tag{7.5}$$

and the dipole matrix element is given by $d_{JJ'}^2 = |\langle J \| \mathbf{d} \| J' \rangle|^2 = \frac{3\pi\epsilon_0\hbar c^3}{\omega_{J'J}^3}(2J'+1)\frac{1}{\tau_{J'J}}$, where (J, J') are for (lower, upper) levels, respectively [202, 21, 130].

For two-level atoms with ground and excited states $|g\rangle, |e\rangle$, the scalar shift U_{scalar} can be approximated by $U_{\text{scalar}} \propto |\mathbf{E}|^2/\delta$ for detunings $\delta = \omega - \omega_a$ large compared to the excited state decay rate Γ, where ω is the electric field angular frequency and ω_a is the $|g\rangle \to |e\rangle$ transition frequency. The ground state will experience a repulsive potential for blue-detuned ($\delta > 0$) electric fields, and an attractive potential for red-detuned ($\delta < 0$) electric fields. The scalar dynamic polarizability $\alpha^{(0)}$ is

in general different for the states $|g\rangle$ and $|e\rangle$ resulting in a differential scalar shift and a mismatch of the ground and excited state potentials. For the typically anti-trapped excited state, near-resonant driving of the transition by an additional beam with frequency $\omega_2 \simeq \omega_a$ can cause significant heating of a trapped atom [53]. This situation can be remedied by the use of "magic" wavelengths for which $\alpha^{(0)}_{|g\rangle} = \alpha^{(0)}_{|e\rangle}$ [258, 133, 121, 162].

The vector term $\hat{H}_1$ of Eq. (7.1) induces a Zeeman-like splitting proportional to a projection of the total atomic angular momentum $\mathbf{F}$ and arises from a so-called "fictitious magnetic field" proportional to the ellipticity of the electric field [71]. For an elliptically polarized beam, the vector shift can be as large as the scalar shift, and can, for example, be used to cancel the differential light shifts of Rubidium atoms confined in a 3D optical lattice [43].

The last term $\hat{H}_2$ in Eq. (7.1) represents the tensor shift. It vanishes for atoms with total angular momentum $F = 1/2$ [87]. In the case of the D_2 transition of Cs that we consider here, it will depend only on the electronic angular momentum $\hat{\mathbf{J}}$ for detunings large compared to the $6P_{3/2}$ excited state hyperfine structure, and vanish for $J = \frac{1}{2}$ [60, 87]. It will therefore only act on the excited state of the Cs D_2 transition, inducing shifts on the Zeeman $m_{F'}$ sublevels proportional to $m^2_{F'}$.

7.2.4 Cancellation of the vector shifts

In the trapping beams configuration shown in Fig. 7.1 c) (i), which is the configuration of Ref. [248], the properties shown in Figs. 3.7 and 3.8 were used to cancel the vector shifts of ground and excited m_F states in Cs for the pair of red-detuned trapping beams. However, vector shifts due to the single blue-detuned beam were zero only for $\phi = \varphi_0,\ \varphi_0 + \pi$ (φ_0 indicates the polarization axis for the beam relative to the x axis). Although the atoms are trapped at $\phi = \varphi_0,\ \varphi_0 + \pi$, inevitable fluctuations of the atom position will lead to non-zero vector light shifts of both ground and excited states.

The scheme in Fig. 7.1 c) (ii) allows for the use of reduced power for the blue-detuned beams as compared to Fig. 7.1 c) (i) but with the consequence of large vector shifts from the ellipticity of the electric field even for $\phi = 0$. We will therefore not consider this scheme in the following sections.

By contrast, the vector shifts of both the ground and excited states can be canceled for both the red and blue-detuned fields by using pairs of counter-propagating beams, as shown in Fig. 7.1 a). In the $x - z$ plane, the vector shift for each pair becomes $\hat{H}_1 \propto (\alpha^{(1)}(\omega^{(\mathrm{fwd})}) - \alpha^{(1)}(\omega^{(\mathrm{bwd})}))\frac{\hat{F}_y}{F}$ with $\omega^{(\mathrm{fwd})} \simeq \omega^{(\mathrm{bwd})}$, where $\omega^{(\mathrm{fwd,bwd})}$ are the angular frequencies for the forward and backward propagating beams, and $\delta \pm \delta_{fb}/2$ are their detunings from the atomic transition frequency ω_a, with

two-photon detuning $\delta_{fb} = \omega^{(\mathrm{fwd})} - \omega^{(\mathrm{bwd})}$. For an atom in the $x-z$ plane, the total electric field is also contained in the $x-z$ plane, such that the scalar product $\left(\hat{\mathbf{E}}^{(-)} \times \hat{\mathbf{E}}^{(+)}\right) \cdot \hat{\mathbf{F}}$ in Eq. (7.1) is proportional to $\hat{F}_y$.

In the case of the red-detuned lattice, $\omega_{\mathrm{red}}^{(\mathrm{fwd})} = \omega_{\mathrm{red}}^{(\mathrm{bwd})}$ and $\hat{H}_1^{(\mathrm{red})} = 0$, precisely as in Ref. [248]. Adding a blue-detuned lattice with $\delta_{fb} = 0$ would result in two superimposed lattices with unmatched spatial periods $2\pi/\beta_{11}^{\mathrm{red}}$, $2\pi/\beta_{11}^{\mathrm{blue}}$. To avoid this effect, the interference between the counter-propagating blue-detuned fields $\mathbf{E}_{\mathrm{blue}}^{(\mathrm{fwd})}$ and $\mathbf{E}_{\mathrm{blue}}^{(\mathrm{bwd})}$ can be averaged over times short compared to the time scale of the motional and internal dynamics of a trapped atom by offsetting the frequencies of the two fields by $\delta_{fb} \gg (\omega_{\mathrm{trap}}, \delta_{\mathrm{hfs}})$, where ω_{trap} and δ_{hfs} are the trap angular frequency and the hyperfine splitting for the ground state, respectively. This will also suppress parametric heating due to intensity modulation [209].

For $\omega_{\mathrm{blue}}^{(\mathrm{fwd,bwd})} = \omega_a + (\delta \pm \delta_{fb}/2)$, we achieve a vector shift cancellation for the blue-detuned field to the first order in $1/\delta$, with second order terms given by:

$$\hat{H}_1^{(\mathrm{blue})} \propto \frac{\delta_{fb}}{\delta^2} \frac{\hat{F}_y}{F} + \mathcal{O}(1/\delta^3). \tag{7.6}$$

For typical values of $\delta = 85$ THz and $\delta_{fb} = 30$ GHz, $\delta_{fb}/\delta = 3.5 \times 10^{-4}$.

7.2.5 Magic wavelengths for an evanescent field trap

To make the nanofiber trap state-insensitive, it is necessary to cancel the differential scalar shift $\delta U_{\mathrm{scalar}}$ of the $6S_{1/2}$ and $6P_{3/2}$ states by operating the trap at the magic wavelengths, as proposed in Ref. [128], in which only the effects of the scalar and tensor shifts were considered. Here we deal with the full complexity of the vector field $\mathbf{E}(\mathbf{r})$ and the resulting vector light shifts. We numerically determine the red-detuned and blue-detuned magic wavelengths for the $6S_{1/2} \rightarrow 6P_{3/2}$ transition, following the procedure described in Refs. [258, 162, 122, 12] with the corrections described in [64] implemented. The results from [64] for the blue-detuned and red-detuned magic wavelengths around 685 nm and 935 nm are shown in Fig. 7.2 (iii) and (iv) respectively.

Our calculation includes the contributions of all the hyperfine levels F and Zeeman sublevels m_F of the atom electronic states $\{6S_{1/2}, \cdots, 15S_{1/2}\}$, $\{6P_{1/2}, \cdots, 11P_{1/2}\}$, $\{6P_{3/2}, \cdots, 11P_{3/2}\}$, $\{6D_{3/2}, \cdots, 11D_{3/2}\}$, and $\{6D_{5/2}, \cdots, 11D_{5/2}\}$. The effect of the tensor shifts on the $6P_{3/2}$ excited state is manifest in the quadratic splitting of the $m_{F'}$ sublevels (Fig. 7.2 (iii)-(iv)). We find a red-detuned magic-wavelength located around 935 nm, in accordance with the previously published values [162, 12]. In the following sections, we will use the value $\lambda_{\mathrm{red}} = 935.3$ nm, which cancels

δU_{scalar} for the $6P_{3/2}$ excited state $|F' = 4, m_{F'} = 0\rangle$. We choose $F' = 4$ due to its relevance to coherent two-photons processes [31, 45, 98]. There are several blue-detuned magic wavelengths [128, 12]. For our trap, we use the magic wavelength λ_{blue} at approximately 685 nm [128]. Since this is the second closest blue-detuned magic wavelength to 852 nm, it has the second highest ground-state polarizability and therefore requires the second lowest optical intensity to generate the required trapping potential (we do not consider the magic wavelength at 792 nm, as it is too close to the $8S_{1/2}$ to $6P_{3/2}$ transition at 794 nm). We note that we have neglected higher order processes in our analysis, including two-photon and electric quadrupole transitions, near 685 nm [62].

Note that there were errors in our initial calculation in [142], which led to the magic wavelength values $\lambda_{\text{red}} = 937.1$ nm and $\lambda_{\text{blue}} = 686.1$ nm. These are the wavelengths used in our nanofiber trap experiment. Correction to our calculation [64] led to the correct magic wavelength values $\lambda_{\text{red}} = 935.3$ nm and $\lambda_{\text{blue}} = 684.9$ nm. The equations and plots shown in this chapter are based on the corrected result [64]. We calculate the trap potential for our experiment using the corrected equations [64], for the actual wavelengths used in the experiment, which were $\lambda_{\text{red}} = 937.1$ nm and $\lambda_{\text{blue}} = 686.1$ nm.

7.2.6 Trap potential and compensation comparison

Using the light shift Hamiltonian in the dipole approximation, Eq. (7.1), with the electric field and polarization profile of the nanofiber evanescent field, we analyze the adiabatic potentials for the nanofiber trap for a Cs atom in its $6S_{1/2}$ ground and $6P_{3/2}$ excited states. For a specific atomic state of Cs, the total atomic trap potential U_{trap} consists of the total light-shift potential U_{ls} calculated from the full Stark shift Hamiltonian (Eq. (7.1)), as well as the surface interaction potential of an atom with the dielectric waveguide U_{surface}, namely

$$U_{\text{trap}} = U_{\text{ls}} + U_{\text{surface}}. \tag{7.7}$$

The Casimir-Polder interaction between the atom and dielectric surface has a significant effect on the atomic motion at distance scales near 100 nm [5, 231, 32, 207, 103]. The surface potential of a ground state Cs atom near a planar dielectric surface can be reasonably approximated by the van der Waals potential which decays as d^{-3}, where $d = r - a$:

$$U_{\text{surface}} = -\frac{C_3}{d^3}, \tag{7.8}$$

where we use $C_3(6S_{1/2})/h = 1.16$ kHz μm^3 [228]. Because the retarded Casimir-Polder forces (d^{-4} scaling) decrease faster away from the surface than the van der Waals forces, using U_{surface} overestimates the surface interaction at the trap location $d \approx$ 200 nm. Additionally, the curvature of the nanofiber cylindrical geometry reduces the potential strength even further [228, 74]. The d^{-3} scaling of the van der Waals expression for a planar surface is therefore an overestimate of the actual surface potential. We use it for simplicity in the calculations presented here, with more complete expressions for Cs presented in Ref. [228]. Furthermore, we neglect any dependence on the $m_{F'}$ sublevels of the excited state $6P_{3/2}$, and simply approximate $C_3(6P_{3/2}) \approx 2\ C_3(6S_{1/2})$ [144]. We estimate that the corrections added by the retarded potential and the surface curvature should be negligible at the trap location, as the surface potential falls off faster than the light potential, as is further discussed in [142].

We calculate the adiabatic potential of Eq. (7.7) by diagonalizing the total interaction Hamiltonian $\hat{H} = \hat{H}_{\text{ls}} + \hat{H}_{\text{surface}}$ at each point in space, where $\hat{H}_{\text{surface}}$ is the scalar surface Hamiltonian. At each point $\mathbf{r}(r, \phi, z)$, we obtain a set of eigenstates and the corresponding eigenenergies as shown in Fig. 7.2 and Fig. 7.3. These eigenstates are superpositions of the $|F, m_F\rangle$ bare Zeeman sublevels. Due to the complex polarization of the trapping fields, the energy eigenstates are not necessarily eigenstates of any projection of the angular momentum operator. The trap potential results are shown in Fig. 7.2 with comparison between the non-compensated and magic-compensated schemes, discussed in the following sections.

7.2.6.1 Trap potential without compensation scheme

Figure 7.2 shows two sets of results (color coded by orange and cyan lines) for the two configurations shown in Fig. 7.2 (i) and (ii) respectively. For the orange color coded configuration, part (i), we consider the trapping parameters for the experiment [248]. Here, the two-color evanescent trap is constructed using a pair of counter-propagating x-polarized ($\varphi_0 = 0$) red-detuned beams $\mathbf{E}_{\text{red}} = \mathbf{E}_{\text{red}}^{(\text{fwd})} + \mathbf{E}_{\text{red}}^{(\text{bwd})}$ ($P_{\text{red}} = 2 \times 2.2$ mW) at $\lambda_{\text{red}} = 1064$ nm, forming an optical lattice, and a single repulsive y-polarized ($\varphi_0 = \pi/2$) blue-detuned beam $\mathbf{E}_{\text{blue}}$ ($P_{\text{blue}} = 25$ mW) at $\lambda_{\text{blue}} = 780$ nm. The SiO_2 tapered optical fiber has a radius $a = 250$ nm in the trapping region.

Fig. 7.2 b) first panel shows the radial trapping potential $U_{\text{trap}}(r, \phi, z)$ of the ground states $F = 3$ and $F = 4$ of $6S_{1/2}$ and excited states $F' = 4$ of $6P_{3/2}$, for $z = 0$ and $\phi = 0$ (x-axis). The energy sublevels of the ground states at the trap location ($\phi = 0$) are degenerate, as both trapping fields are linearly polarized as illustrated in Fig. 3.7. The excited state energy sublevels are shifted due to

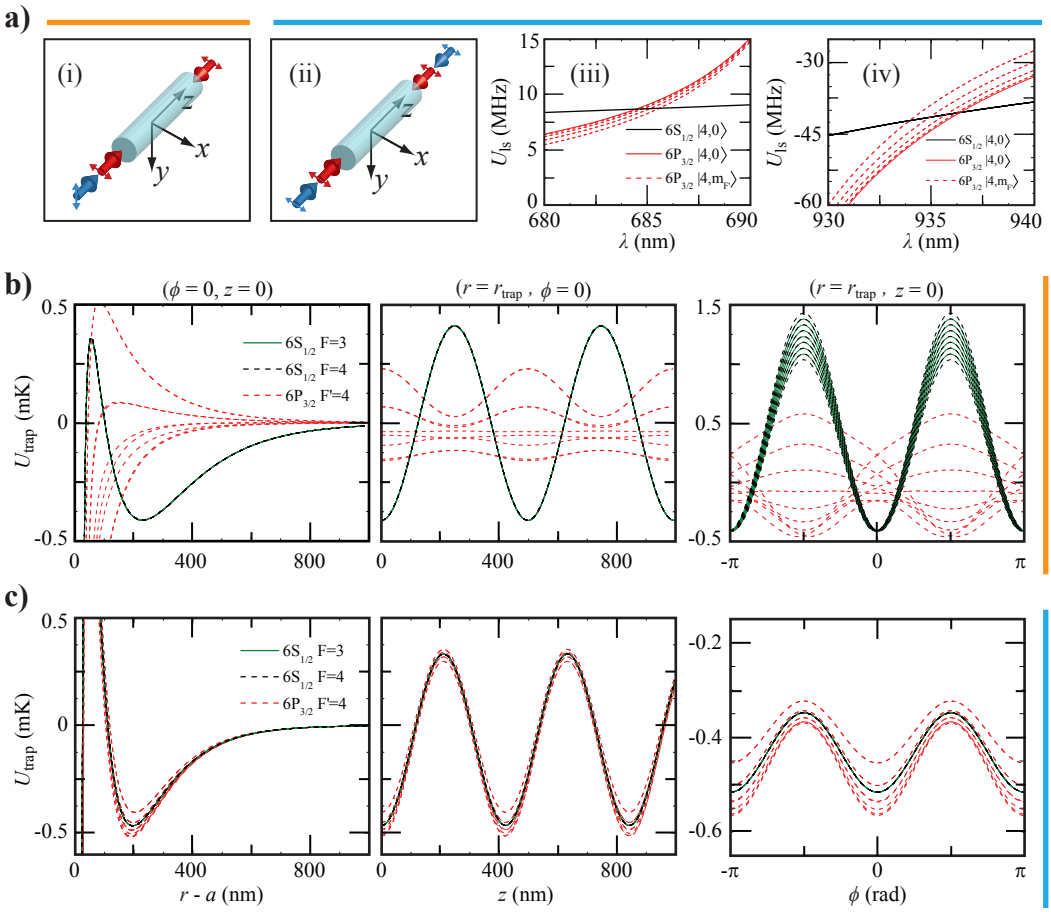

Figure 7.2: **Effectiveness of the magic-compensated trapping scheme. a)** (i) Nanofiber trap scheme of [248] (orange color code); (ii) Our magic-compensated trap scheme (cyan color code), with magic wavelengths for the $6S_{1/2}, F = 4 \rightarrow 6P_{3/2}, F' = 4$ transition of the Cs D_2 line shown in (iii) and (iv). The light shifts U_{ls} are for a linearly polarized beam with constant intensity 2.9×10^9 W m^{-2} around (iii) the blue-detuned magic wavelength at $\lambda_{\text{blue}} \simeq 684.9$ nm and (iv) red-detuned magic wavelength at $\lambda_{\text{red}} \simeq 935.3$ nm. **b)** Atom energy levels for the configuration shown in (i) of a), orange color code, using parameters of [248]. Trap minimum is located at $r_{\text{trap}} - a = 230$ nm from the fiber surface, where the fiber radius is $a = 250$ nm. **c)** Atom energy levels for the magic-compensated scheme shown in (ii) of a), cyan color code, using the parameters $\lambda_{\text{red}} = 935.3$ nm, $P_{\text{red}} = 2\times$ 0.95 mW and $\lambda_{\text{blue}} = 684.9$ nm, $P_{\text{blue}} = 2\times$ 16 mW. Trap minimum is located at $r_{\text{trap}} - a = 200$ nm from the fiber surface, where the fiber radius is $a = 250$ nm. **b-c)** The energy sublevels of the ground states $F = 3$ and $F = 4$ of $6S_{1/2}$ are shown as solid green and dashed black curves, and the $F' = 4$ sublevels of the electronically excited state ($6P_{3/2}$) are shown as red dashed curves. In the first column are radial trap potentials ($\phi = z = 0$); second column, axial trap potentials ($r = r_{\text{trap}}, \phi = 0$); and third column, azimuthal trap potentials ($r = r_{\text{trap}}, z = 0$). In c), the compensation configuration leads to suppression of energy level splitting spreads due to vector shifts of the blue-detuned beams, and the use of magic wavelengths minimizes differential energy shifts between the ground and excited states.

the vector and tensor shifts. The trap depth for the ground state is $U_{\text{depth}} = -0.4$ mK, located at $r - a \simeq 230$ nm and $\phi = 0$, whereas the excited states are not trapped at all. The axial dependence of the trap potential (at $r = r_{\text{trap}} = a + 230$ nm, $\phi = 0$) is shown in the second panel of Fig. 7.2 b).

The azimuthal dependence of the trap potential reveals a significant inhomogeneous broadening of the energy sublevels due to the ellipticity of $\mathbf{E}_{\text{blue}}$ for $\phi \neq 0, \pi$ (see third panel of Fig. 7.2 b)). To estimate this broadening, we assume that the potential is harmonic around the trap minimum. By fitting the ground state $F = 3$ potential with a harmonic potential around $\phi = \pi$, we obtain an azimuthal trapping frequency $\nu_{\text{trap}_\phi} \simeq 150$ kHz. For an atom in its azimuthal motional ground state $|n\rangle_\phi = |0\rangle_\phi$ in such a potential, the half-width σ_{r_ϕ} of the corresponding single-atom distribution is given by $\sigma_{r_\phi} = \langle (r\phi)^2 \rangle \simeq r_{\text{trap}}\sigma_\phi = \sqrt{\frac{\hbar}{4\pi m \nu_{\text{trap}_\phi}}} \simeq 16$ nm (or azimuthal half-width of $\sigma_\phi \simeq 2^\circ$). This leads to fast decoherence of the hyperfine and Zeeman levels, even with ground state cooling. Specifically, we estimate a spin-wave coherence time $\tau_m = 1/\delta\nu_\phi \lesssim 5$ μs, derived from the $\delta\nu_\phi = 200$ kHz splitting between the sublevels of the $F = 4$ atomic ground state 16 nm away from the trap minimum. This is significantly limited compared to the quantum memory performances of atomic ensembles in optical lattices (see, e.g., [192]).

As evident from the plots in Fig. 7.2 b) for the configuration of Fig. 7.2 (i), color-coded with orange lines, the excited states are untrapped in all directions except along the fiber axis z for the parameters of Ref. [248]. An atom excited to these untrapped potentials will experience dipole-force fluctuations, leading to heating [53] and preventing near-resonant driving of the optical transition [247].

7.2.6.2 Trap potential with compensation scheme

Fig. 7.2 a) (ii)-(iv) shows the "magic compensation" scheme that utilizes two pairs of counter-propagating blue- and red-detuned beams all linearly polarized along the x-axis, as shown in Fig. 7.2 a) (ii), with magic wavelengths around 685 nm (we use $\lambda_{\text{blue}} = 684.9$ nm) and 935 nm (we use $\lambda_{\text{red}} = 935.3$ nm) respectively, shown in Fig. 7.2 a) (iii)-(iv). The trap potential for this scheme (color coded by blue lines) are shown in Fig. 7.2 c). We see that the use of magic wavelengths and a compensation scheme that suppresses electric field ellipticities reduces inhomogeneous broadening of the Zeeman sublevels in a nanofiber trap.

For this trap, we use a pair of counter-propagating x-polarized ($\varphi_0 = 0$) red-detuned beams $\mathbf{E}_{\text{red}} = \mathbf{E}_{\text{red}}^{(\text{fwd})} + \mathbf{E}_{\text{red}}^{(\text{bwd})}$ ($P_{\text{red}} = 2 \times 0.95$ mW) at the "magic" wavelength $\lambda_{\text{red}} = 935.3$ nm, forming a 1-D optical lattice. Counter-propagating, x-polarized blue-detuned beams at the second "magic"

wavelength $\lambda_{\text{blue}} = 684.9$ nm are used with a power $P_{\text{blue}} = 2 \times 16$ mW. The resulting interference is averaged out by detuning the beams by $\delta_{fb} = 30$ GHz, as explained in Section 7.2.4, leading to a first-order cancellation of vector light shifts as expressed by Eq. (7.6). The beam intensities are chosen to generate a trap of similar depth as the one demonstrated in Ref. [248]. The resulting adiabatic potential U_{trap} allows for state-insensitive 3D confinement of cold Cs atoms around a SiO_2 nanofiber of radius $a = 250$ nm.

In the first panel of Fig. 7.2 c), we show the radial trapping potential $U_{\text{trap}}(r, \phi, z)$ of the ground and excited states for $z = 0$, $\phi = 0$ (x-axis). Because the trapping fields are now effectively linearly polarized, the ground states are degenerate at both $\phi = 0$ and $\phi = \pi/2$. In contrast to a non-magic wavelength trap, the excited states are trapped with gradients that closely map that of the ground states. The sublevels of $6P_{3/2}$ are still non-degenerate due to the tensor shifts. For P_{red}, P_{blue} specified above, we find that the trap depth is $U_{\text{depth}} = -0.4$ mK, located at $r - a \simeq r_{\text{trap}} - a = 210$ nm and $\phi = 0, \pi$. The axial potentials are shown in the second panel of Fig. 7.2 c), showing confinement for both the ground and excited states.

The azimuthal confinement of the atoms is shown in the third panel of Fig. 7.2 c). The trap depth is reduced compared to the corresponding uncompensated potential shown just above the plot in row b) of the figure, due to the use of parallel polarizations for the trapping beams. This could be overcome by using higher trapping power, to make the trap deeper in all directions. Using perpendicular polarizations for the blue-detuned and red-detuned beams would unfortunately require prohibitively high power at 685 nm. In contrast to the configuration shown in Fig. 7.2 a) (i), the orange color coded case, the inhomogeneous Zeeman broadening from the ellipticity of $\mathbf{E}_{\text{blue}}$ is greatly reduced thanks to the compensation scheme of Fig. 7.2 a) (ii)-(iv), cyan color coded case. It is non-zero, however, as expressed by Eq. (7.6). The remaining splitting of the $F = 4$ ground state is $\delta_\nu \approx 700$ Hz, limiting the coherence time to $\tau \lesssim 1/\delta_\nu = 1.4$ ms.

In the case of perfect cancellation of the vector shift with $\delta_{fb} = 0$, a residual non-zero ground state splitting $\delta\nu_\phi$ would still arise from the different scalar dynamic polarizabilities of the $6S_{1/2}$ $F = 3$ and $F = 4$ ground states [202]. For atoms in their azimuthal motional ground state $|n\rangle_\phi = |0\rangle_\phi$, the single-atom distribution half-width is $\sigma_{r_\phi} \simeq 30$ nm (or $\sigma_\phi \simeq 4°$) with azimuthal trap frequency $\nu_{\text{trap}_\phi} \simeq 44$ kHz obtained from a harmonic fit of the potential around $\phi = \pi$. We estimate a spin-wave coherence time $\tau_m = 1/\Delta(\delta\nu_\phi) \leq 30$ ms, coming from the spread $\Delta(\delta\nu_\phi) = \delta\nu_\phi(\phi = \pi) - \delta\nu_\phi(\phi = \pi + \sigma_\phi) \approx 30$ Hz of the atomic ground states for the $F = 3 \rightarrow F = 4$ transition frequency.

We note that the longest achievable coherence time in the "magic compensated" adiabatic poten-

tial in the absence of ground-state splitting $\delta\nu_\phi$ would be limited by spontaneous Raman scattering driven by the trapping beams [162].

As evident from the plots in Fig. 7.2 c) for the "magic compensated" scheme shown in Fig. 7.2 (ii), with magic wavelengths, color-coded with blue lines, the excited states are trapped in all directions. This results in greatly suppressed dipole-force fluctuations, allowing for on-resonance driving of the optical transition.

7.2.6.3 Trap potential of nanofiber trap experiment

Figure 7.3 shows the trap potential for the configuration and parameters used in our experimental demonstration discussed in Sec. 7.4 using a nanofiber that we fabricated as discussed in Sec. 7.3. The trap potential consists of a pair of counter-propagating x-polarized ($\varphi_0 = 0$) red-detuned beams ($P_{\rm red} = 2 \times 0.4$ mW at $\lambda_{\rm red} = 937.1$ nm), and counter-propagating, x-polarized blue-detuned beams ($P_{\rm blue} = 2 \times 5$ mW at $\lambda_{\rm blue} = 686.1$ nm), detuned by $\delta_{\rm fb} = 382$ GHz relative to each other, which averaged out the blue-detuned beams interference pattern.

Note that there were errors in our initial calculation in [142], which led to the magic wavelength values $\lambda_{\rm red} = 937.1$ nm and $\lambda_{\rm blue} = 686.1$ nm, which were the wavelengths used in our experiment. Correction to our calculation [64] later led to the correct magic wavelength values $\lambda_{\rm red} = 935.3$ nm and $\lambda_{\rm blue} = 684.9$ nm. The calculation for the trap potential for our experiment is based on the corrected equations [64], for the actual wavelengths used in the experiment, which were $\lambda_{\rm red} = 937.1$ nm and $\lambda_{\rm blue} = 686.1$ nm.

The silica nanofiber radius used in our experiment is $a = 215$ nm. These parameters lead to vector light shifts suppression by $\delta_{fb}/\delta_{\rm blue} \simeq 4 \times 10^{-3}$, and the resulting potential $U_{\rm trap}$ allows for state-insensitive, 3D confinement of Cs atoms along a silica nanofiber for the $6S_{1/2}$ ground and $6P_{3/2}$ excited states. The trap depth at the minimum is $U_{\rm trap} = -0.27$ mK located about 215 nm from the fiber surface, with trap frequencies $\{\nu_\rho, \nu_z, \nu_\phi\}/2\pi = \{199, 273, 35\}$ kHz. The contour plots for the ground-state $6S_{1/2}$, F=4 in atomic cesium and cross-sectional plots for the substates of the ground-state $6S_{1/2}$, F=4, and the excited-state $6P_{3/2}$, F'=5, are shown by the black and red-dashed curves in Fig. 7.3 respectively.

7.3 Fabrication of a tapered nanofiber

In this section we describe the fabrication of a tapered optical nanofiber for our nanofiber atom trap as discussed in Sec. 7.2 and Sec. 7.4. There are a number of goals or specifications that are required

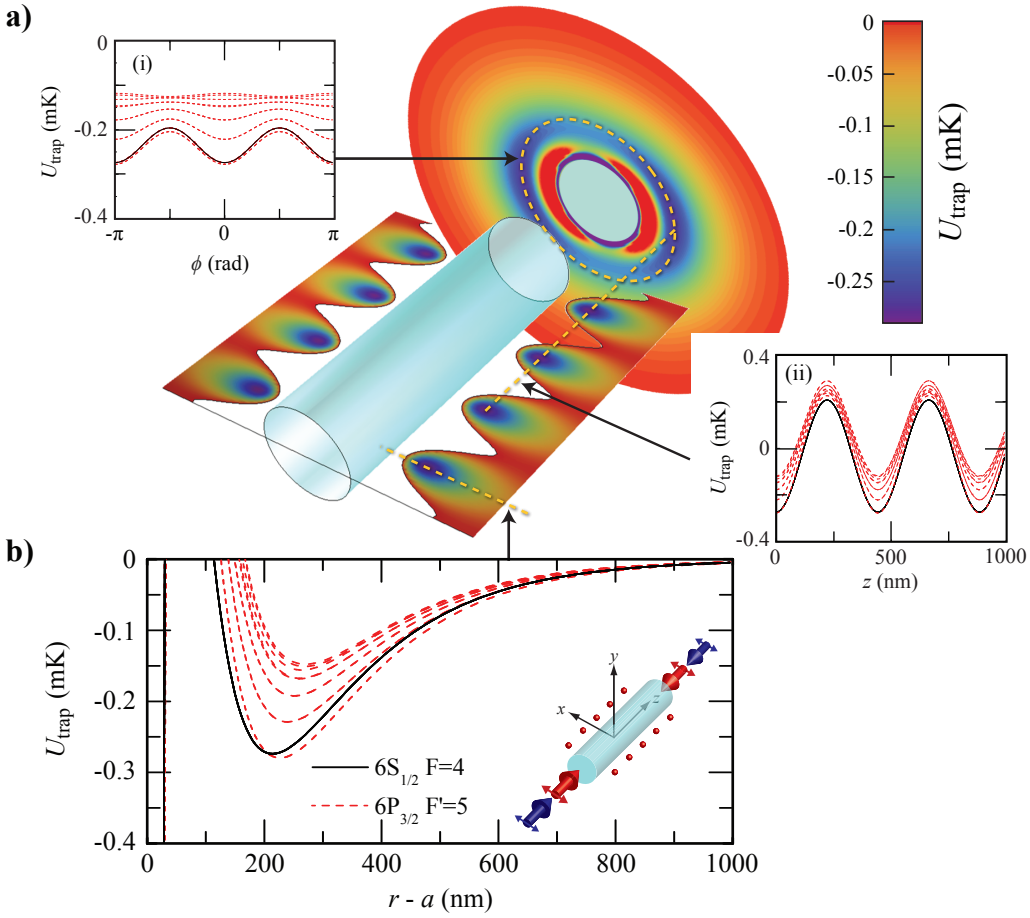

Figure 7.3: **Trapping potential for nanofiber atom trap experiment with magic-compensated scheme. a-b)** Adiabatic trapping potential $U_{\rm trap}$ for a state-insensitive, compensated nanofiber trap for the $6S_{1/2}, F = 4$ states in atomic Cs outside of a cylindrical waveguide of radius $a = 215$ nm. Contour plots show $U_{\rm trap}$ for the ground state $F = 4$ of $6S_{1/2}$. For the cross-sectional plots, $U_{\rm trap}$ for the substates of the ground level $F = 4$ of $6S_{1/2}$ (excited level $F' = 5$ of $6P_{3/2}$) are shown as black (red-dashed) curves. **(a)(i)** azimuthal $U_{\rm trap}(\phi)$, **(ii)** axial $U_{\rm trap}(z)$ and **(b)** radial $U_{\rm trap}(r - a)$ trapping potentials. The trap minimum for $6S_{1/2}$ is located at about 215 nm from the fiber surface. Input polarizations for the trapping beams are denoted by the red and blue arrows in the inset in (b). Here we utilize a pair of counter-propagating x-polarized ($\varphi_0 = 0$) red-detuned beams ($P_{\rm red} = 2 \times 0.4$ mW) at $\lambda_{\rm red} = 937.1$ nm, and counter-propagating, x-polarized blue-detuned beams ($P_{\rm blue} = 2 \times 5$ mW) at $\lambda_{\rm blue} = 686.1$ nm as described in Sec. 7.4. The resulting interference is averaged out by detuning the beams to $\delta_{fb} = 382$ GHz. Due to the complex polarizations of the trapping fields, the energy levels are not the eigenstates of the angular momentum operators, but rather superposition states of the Zeeman sublevels. Note that there were errors in our initial calculation in [142], which led to the magic wavelength values $\lambda_{\rm red} = 937.1$ nm and $\lambda_{\rm blue} = 686.1$ nm, used in our experiment. The correct magic wavelength values are $\lambda_{\rm red} = 935.3$ nm and $\lambda_{\rm blue} = 684.9$ nm [64]. The plots in this figure are based on the corrected equations [64], for the actual wavelengths used in our experiment, $\lambda_{\rm red} = 937.1$ nm and $\lambda_{\rm blue} = 686.1$ nm.

for the realization of our magic-compensated scheme nanofiber atom trap:

- Firstly, the nanofiber needs to have a small diameter of $\approx$ 400 nm, which supports a single mode at $\lambda_{\text{blue}} = 685$ nm. We note that the fabrication becomes increasingly challenging as the diameter decreases, as its sensitivity to imperfections increases. The tapered fiber shape profile, particularly the nanofiber diameter, needs to be well-controlled such that it can be fabricated with high repeatability and sufficiently precise prediction, as the nanofiber diameter determines the shape of the guided mode, hence the dipole trap potential.

- Secondly, the shape profile determines the optical transmission efficiency of the tapered nanofiber. The ideal shape is an adiabatic one, where during the transition from large-diameter $\approx$ 125 μm standard single-mode fiber to the tapering region and then small-diameter $\approx$ 400 nm nanofiber, the optical excitation stays at the lowest order fundamental mode, with negligible higher-order modes excited. Any higher-order mode excited will leak out of the tapered nanofiber where there is a sufficiently thin fiber diameter region that does not support that mode. This then contributes to optical power loss.

- Thirdly, the tapered nanofiber needs to be able to handle a relatively large amount of optical power ($\sim$ 10 mW) without breaking/melting. As the nanofiber is positioned inside an ultra-high-vacuum (UHV) environment, there is limited thermal conductivity available, which places a strict constraints on the maximum temperature at any part of the fused silica nanofiber. Although the melting temperature of fused silica is around 2000 Kelvin and it will be difficult to heat up the entire tapered fiber to this temperature, small scattering such as from dust particles on the nanofiber surface could heat it up beyond the melting temperature with as little as 10 μW optical power inside the UHV environment. This is because there is a significant optical intensity present in the evanescent field of the nanofiber mode, extending relatively far away from the nanofiber's surface, which provides the energy to the scatterer. This combined with the highly limited thermal conductivity via conduction through the nanometer-sized nanofiber, and absence of convection dissipation channel inside the UHV chamber, requires absence of these dust particles, which could otherwise lead to the melting of the glass. We note that these melting/breaking points occur locally, at the scatterer particle location, and consequently even one of these dust particles would be sufficient to break the nanofiber.

In this section, we discuss how we achieved the three requirements above.

7.3.1 Nanofiber fabrication setup

Figure 7.4 shows our nanofiber fabrication setup, which at its heart consists of two main components, namely a heater (in our case a hydrogen-oxygen torch) and a set of motorized translation stages that pull both ends of a standard optical fiber apart as it is heated. To create a smooth, slowly varying taper diameter, avoiding abrupt steep slopes, a relatively large effective heating region is produced by oscillating the fiber-pulling stage relative to the torch flame, the so-called flame brush technique [25, 8, 229, 249, 157]. In our case, we have an effective heating region of 6 mm created by oscillating the fiber relative to the stationary torch flame of size $\lesssim 1$ mm^2. Refering to Fig. 7.4 a) and b), we will now discuss each component as indicated by the number-letter labels. The set of components labeled 1 provides vertical, longitudinal, and tilt alignments of the torch assembly (component set 2). While the vertical- and tilt-mounts (1a) and (1c) are manually adjustable (from Edmund Optics), the longitudinal-mount (1b) is motorized to allow automated positioning of the flame into and out of the nanofiber region (from Thorlabs). The torch assembly consists of a custom-made torch (National Torch from Premier Industries, custom-modified Model 8R Rider torch for H2/O2) that mixes H2 and O2 (2a) attached to an elbow (2b) with a 1-orifice nozzle (orifice diameter ≈ 1.2 mm) at the end labeled by 2c. The elbow and nozzle are from National Torch/Premier Industries, MEH-series elbow and MSOX-2 nozzle (single orifice of diameter 0.047"). The top motorized stage (3b) moves away from the torch to pull the fiber (4b) that is clamped by magnetic clamps (3d). The bottom motorized stage (3a) oscillates in addition to moving away from the torch, providing both fiber pulling and an relatively large effective heating region as discussed above. The two motorized stages 3a and 3b are Newport models XML210 and XMS160 respectively, controlled by XPS-C2 controller with two drivers XPS-DRV02 all from Newport. All of the adapter plates between motors and mounts are home-machined with aluminium material. We note that the fiber (630-HP single-mode bare fiber from Nufern, with 250 μm buffer) is prepared by wiping it with an isopropyl alcohol, and stripping with a thermal stripper (4a) in Fig. 7.4 c) (iii). The thermal stripper is from Jonard Industries, model TSFB-125. As the fiber is pulled, a laser is injected into the fiber and monitored in real-time by a photodetector at the cut end of the fiber (4c) in Fig. 7.4 b) (ii). We note that special care must be taken when mounting the bare fiber using the (Thorlabs HFV001) magnetic clamps (3d), to ensure a straight, torsionless, with a very slight tension, mounting. The 'good' mounting feeling

[2]Note that in collaboration with Kiyoul Yang of Vahala group, we have explored taper pulling using a ceramic heater (NTT AT ceramic micro heater CMH-7019, width $\times$ depth $\times$ height $= 19 \times 25 \times 20$ mm, which heats up to a temperature of 1000 to 1600 °C for 2 to 4 Amps driving current), which showed preliminary successes for tapers with waist diameter $\gtrsim 1$ μm. We have not investigated fabrication of smaller-sized tapers. To drive the micro heater, we used Instek APS-1102 ac power source.

comes with practice.

The pulling procedure is as follows. After the mounting of a bare fiber in position (3d), an appropriate amounts of hydrogen and oxygen gasses are supplied (9a) to the H2-O2 torch. This is controlled by two independent gas mass flow controllers (10a), each of which is connected to a gas filter that filters out any contaminants including water molecules (10b), and which are then connected to hydrogen and oxygen tanks (with valves, flash back arresters and regulators). The mass flow controllers (10a) are from Sierra Instruments, series 100, model number C100L-DD-13-OV1-SV1-PV2-V1-S0-C0, and they actively regulate the gas flows with a preset amount (e.g., 360 mL/min for H2, 60 mL/min for O2). After the gases are flowing (torch tip is kept away from the fiber region), the torch is lit. For a given ambient air condition, a torch with only hydrogen gas (no oxygen gas) will lead to a flame of a particular temperature, dependent on the ratio of hydrogen-to-oxygen molecules present in the ambient air. Here, we use oxygen gas to allow tuning of this hydrogen to oxygen stoichiometric ratio, allowing tuning of the flame temperature. To allow deformation of our fused silica fiber, we need to heat the fiber up to above the annealing point (1140° C). We should however not heat it up to the softening point (1665° C), where the fused silica material/fiber will sag under its own weight. Moreover, we should also not exceed 1550° C, because heating beyond this temperature will lead to the formation of beta-quartz SiO_2 crystals following cooling of the heated fused silica back to room temperature [157]. Therefore, a good temperature is to be just slightly below 1550° C, to allow taper pulling with minimal force. In our case, we empirically optimize the hydrogen and oxygen gas flow rates (given our specific torch nozzle and orifice design) to give the best pulling result. Finally we note that the melting temperature of fused silica is 1723° C.

For cleanliness reasons, our fabrication setup is located inside a class-100 cleanhood (8a). Now that we have our fiber mounted and flame on, in the next step we place a small cover (7a) above the fiber as well as lowering the cleanhood fan speed, to avoid strong blowing of the fiber during the pulling process, which could jitter the fiber position causing adverse effects. Rapidly following this, we close our cleanhood door and run the pre-programmed pulling sequence from a computer, which initiates the pulling process. It begins with moving the torch (2c) into the fiber region, and is followed by the pre-programmed sequences for the two motorized stages (3a,3b). The exact trajectories of the pulling motors will be discussed in Sec. 7.3.2. This stage of the pulling process takes about 7-8 minutes, where the temporal and spectral real-time monitoring of the optical output of the fiber goes through phases: single-mode, multi-mode (beat notes in temporal measurement and some Fourier components in spectral measurement), and back to single-mode behavior, as the fiber starts from its

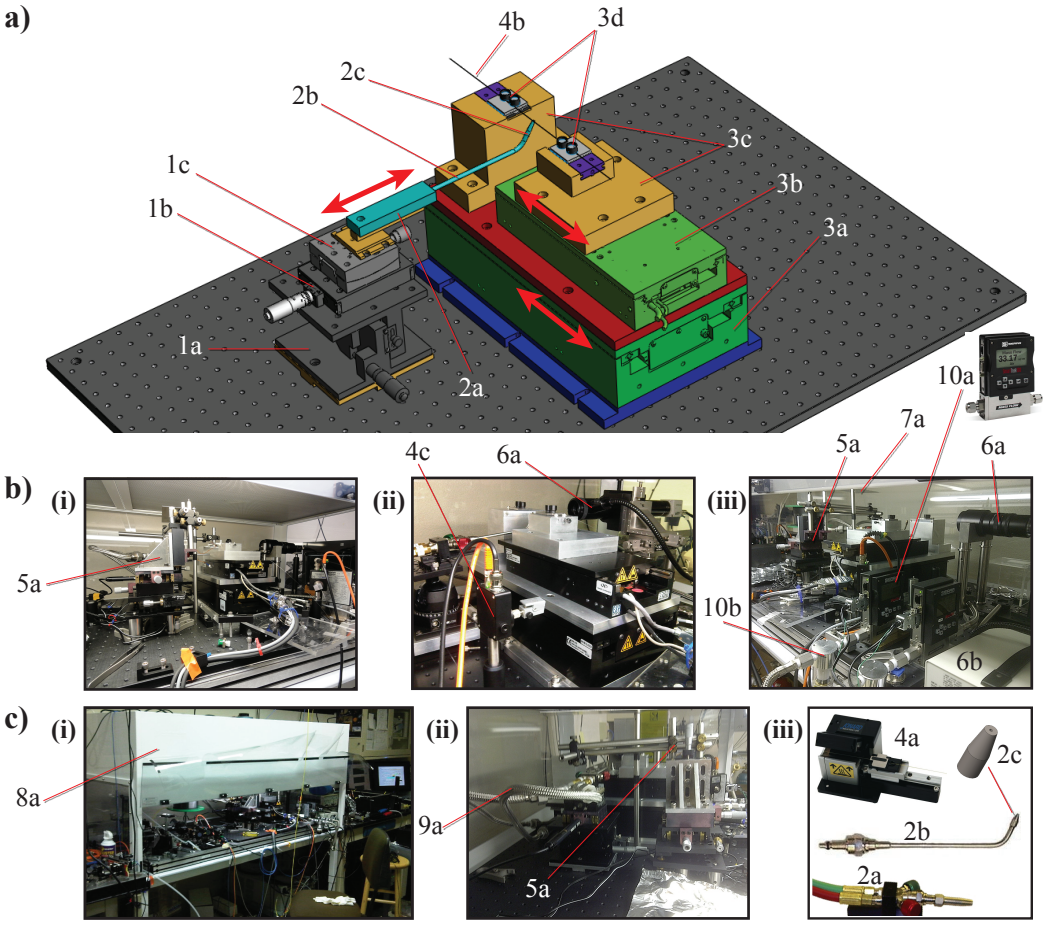

Figure 7.4: **Tapered optical nanofiber fabrication. a)** Schematic of tapered fiber pulling setup. (1a-c): Motorized and manual stages for H_2-O_2 torch mount. (2a-c): Hydrogen-oxygen torch, with a 1.2 mm diameter single-orifice nozzle as shown in part c) (iii) of figure. (3a-b): Computer controlled, high precision motorized linear stages. (3c): Custom aluminium adapter blocks. (3d): Magnetic fiber clamps. (4b): Bare fiber to be tapered. **b-c)** Photographs of setup and components. (5a): Precision manual translation stage used to hold experiment aluminium taper holder during gluing process. (4a): Photodetector monitoring optical power transmission of fiber during pulling. (6a-b): Microscope imaging and illumination. (10a-b): H_2-O_2 gas mass flow controllers and filters. (7a): Air current shield used in pulling process. (8a): Class-100 cleanhood. (9a): Flexible stainless steel braided gas hoses. (4a): Thermal fiber stripper.

initial single-mode geometry, goes to taper geometry that supports higher-order mode, and finally results in nanofiber geometry at the center that only supports a single-mode. Although after the system is well set up and has become stable (i.e., it produces repeatable tapers with well-predictable characteristics) everything is automated, the real-time temporal and spectral optical measurement provides feedback concerning when the tapered fiber becomes single-mode, and, as importantly, the optical transmission efficiency of the finished product. We note that we also monitor the pulling process with a microscope CCD camera imaging setup (6a), illuminated by a standard microscope illumination light (6b). After the pulling sequence is completed, the flame automatically retracts away from the fiber region, so that no more heating is applied. We then jog for about 55 seconds (with each motor pulling the taper at 0.02 mm/s), to tension the tapered fiber. Note that during the tensioning the fiber is no longer being heated. The transition from loose to tensioned is apparent from the microscope imaging camera.

After the tapered fiber is tensioned, we take out the 'wind shield' (labeled 7a in Fig. 7.4 b) (iii)), and restore the cleanhood fan speed to normal operating speed. The fiber is then glued onto an aluminium fork, as shown in Fig. 7.8 a). The aluminium fork is carefully positioned at the right position with the fork arms' surfaces just coming into contact with the tapered fiber. This is done using a 3D-stage combined with tip-tilt adjustability, shown in Fig. 7.4 labeled 5a, which holds the aluminium fork. For the glue, we used a UV-cured glue from Dymax (OP-4-20632-3ML), applied using a 22 gauge syringe needle, as well as a room-temperature curing two-component premixed ceramic compound from Aremco Products (Ceramabond 835-M), both of which are UHV-vacuum-compatible. We note that while the UV-cured glue is more convenient to apply (as it is much less viscous prior to curing), it has much higher thermal expansion coefficient compared with the Ceramabond compound, which may be important in certain situations.

7.3.2 Trajectories of pulling motors

Figure 7.5 h) shows a side-view diagram of the taper pulling setup placed on top of the (dark gray) breadboard, consisting of the base (heating) motor (i), first adapter aluminium plate (ii), pulling motor (iii), second adapter plate (iv), the fiber (v), and the stationary torch nozle and flame (vi). The initial gap between the two fiber clamps is L0, and the final gap is L1, achieved after the total pulling time t1 = 466 seconds (7 mins 46 seconds). At this final time t1, the top (pulling) motor and the two adapter plates are shown with transparency, where the heating plate is moved a distance zh1 in the negative z_{h} direction, and the pulling plate is moved a distance zp1 in the positive z_{p}

direction. Note that z_{h} and z_{p} represent the displacements of the heating (bottom) and pulling (top) motors respectively with respect to their initial positions, with the positive direction pointing to the right-hand-side in the diagram.

The pre-programmed position and velocity trajectories are shown in Figure 7.5, which are the input instructions pre-programmed into the motor controllers. From these data matrices, generated from Matlab code, the motor controller computes a smooth trajectory (up to the jerk, time derivative of acceleration), with speed stability of 1% and position hysteresis/repeatability of ± 100 nm. Although the position and velocity trajectories are defined up to $t = 817$ seconds, the execution LabView program automatically stops the sequence at $t = \mathrm{t1} = 466$ seconds, a number that we arrived at after empirical optimization. Note that typically, the tapered fiber goes to single-mode (at $\lambda =$ 852 nm) at $t = 449$ seconds, and it goes to single-mode at $\lambda = 687$ nm before $t = 466$ seconds. The position and velocity trajectories for the bottom (heating) motor, z_{h} and v_{h}, are shown in Fig. 7.5 a) and b) respectively, with the first 10 seconds shown in Fig. 7.5 c) and d) respectively. At the turning point of the oscillating bottom (heating) motor, we use a sinusoidal smoothing function, highlighted by (i) in Fig. 7.5 d), shown in Fig. 7.5 f), with a total turning time of 100 ms. This helps in ensuring a smooth oscillation motion of the bottom (heating) motor. The position and velocity trajectories for the top (pulling) motor, z_{p} and v_{p}, are shown in Fig. 7.5 e) and g) respectively. We found that having gradual steps of increasing velocity as shown in Fig. 7.5 g) helps significantly in improving the quality (particularly transmission efficiency) of the taper.

7.3.3 Nanofiber profile

The final shape of a tapered fiber fabricated using the flame brush technique, as in our case, can be modeled as a deformable fused silica cylinder that is pulled at both ends, and heated by a rectangular cross-section hot zone at the center (with width determined by the effective heating region, e.g., 6 mm). Neglecting thermal conduction effects, pulling speed, material imperfections and the non-rectangular hot zone profile, simply by imposing conservation of mass (hence also volume), this model [25] presents a very good approximation to reality. For an initial fiber of radius r_0, rectangular hot zone of width L_{w}, and a total pulling length $\Delta L = L1 - L0 - L_{\mathrm{w}}$, the shape of the tapered fiber is described by an exponentially decaying function [25]:

$$r(z) = r_0.e^{-\frac{\Delta L}{2L_{\mathrm{w}}}z}, \tag{7.9}$$

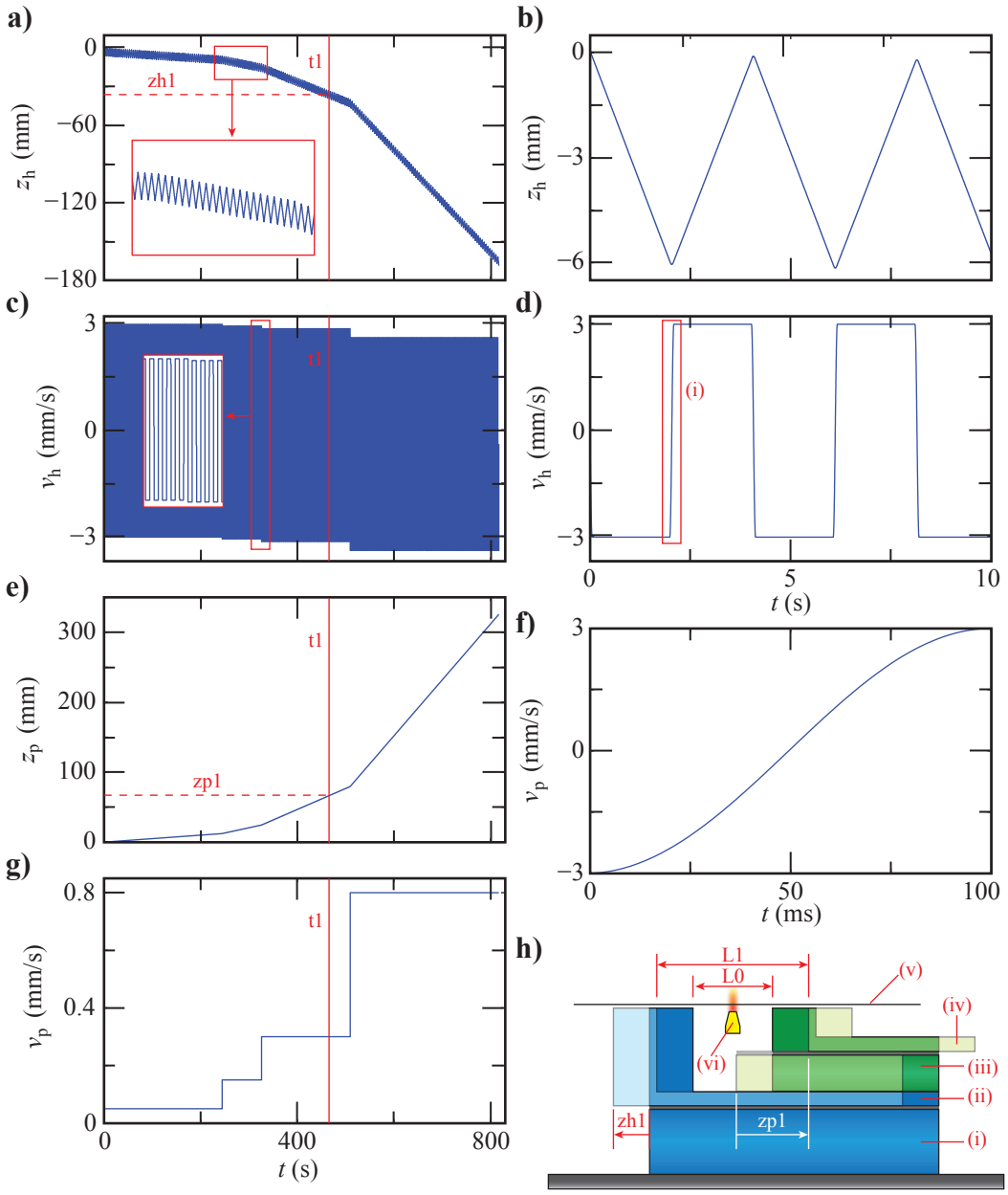

Figure 7.5: **Taper pulling motorized stages position and velocity trajectories. a-g)** Position and velocity trajectories programmed to the heating (i)-(ii) and pulling (iii)-(iv) motors shown in h). **a)** Heating stage position, z_h, as a function of time t, with the first 10 seconds of the sequence shown in b). **c)** Heating stage velocity, v_h, as a function of time t, also shown in d) for the first 10 seconds. **e, g)** Pulling stage position (z_p) and velocity (v_p) trajectories. The insets in a) and c) show expanded views of the plots. In (a,c,e,g), the time t1 corresponds to the optimized end time of the trajectory sequence run used in our nanofiber fabrication, where in the time $t = 0 \rightarrow t =$ t1, z_h moves by zh1 in the negative direction, and z_p moves by zp1 in the positive direction (see part h)). To avoid abrupt motion at the turning points, the heating stage changes direction in velocity with a sinusoidal profile over 100 ms as shown in (i) in d), expanded in f). The computer controller takes all of the position and velocity trajectory inputs and moves the motorized stages with high precision and smooth trajectories up to the jerk (time derivative of acceleration). **h)** The motion of the stages from the start ($t = 0$) to end ($t =$ t1) pulled the fiber (v) heated by the flame (vi) from length L0 to length L1.

where z is the fiber axis, starting from the initial fiber radius r_0 at $z = 0$, exponentially decaying to the nanofiber waist radius $r_{\rm w}$ (at $z = \Delta L/2$), being followed by a constant nanofiber radius $r_{\rm w}$ over the entire effective heating length $L_{\rm w}$ (up to $z = \Delta L/2 + L_{\rm w}$), then increasing with an exponential growth function back to the non-tapered fiber radius r_0 at $z = \Delta L + L_{\rm w}$. For our case, our initial fiber radius (with the buffer stripped) is $r_0 = 62.5$ μm and the total pulling length (including final jogging tensioning part) is $\Delta L = 66.9$ mm. From the pre-programmed base motor oscillation trajectory (discussed in Sec. 7.3.2), treating the flame as a box of hot zone, then $L_{\rm w} =$ 6 mm. We find empirically however that this number needs to be adjusted to $L_{\rm w} = 5.9$ mm, to agree with the actual measured nanofiber waist radius $r_{\rm w} = 215$ nm. This correction is systematic, and it applies to multiple ($\gtrsim 10$) tapered fibers that we characterized, where in all cases a value of $L_{\rm w} = 5.9$ mm leads to good agreement between the theory and measurements. We believe this 0.1 mm correction is attributable to the fact that the flame is not a box of hot zone, but rather it has a certain temperature profile and gradient, especially at the edges. This then leads to an effective heating length of $L_{\rm w} = 5.9$ mm. Using this effective heating length value, we find very good agreement between the theory and scanning electron microscope (SEM) measurements of the taper shape profile. Here, the total end-to-end tapered fiber has the length $L_{\rm total} = \Delta L + L_{\rm w} = L1 - L0$ = 72.8 mm, where L1 and L0 are shown in Fig. 7.5 h).

Figure 7.6 a-b) show hundreds of SEM measurement data of fabricated tapered fiber profiles from our fabricated samples and the theoretical curves discussed above, with $L_{\rm w} = 6$ mm and 5.9 mm for cyan and red curves respectively (in part a) in linear scale and in part b) in logarithmic scale). Fig 7.6 c) gives a closer look at the taper profile around the nanofiber waist, with the theoretical curves (i) in cyan and (ii) in red corresponding to the cases for $L_{\rm w} = 6$ mm and 5.9 mm. The central region yields an average radius $r(z) = 215 \pm 10$ nm for $-3 < z < 3$ mm. We note that the SEM measurement process can have up to about 10% measurement uncertainty (associated with systematic spatial calibration taking into account varying focusing conditions, and variations in image acquisition process), so to estimate the nanofiber waist radius $r_{\rm w}$ of the samples, we averaged the SEM data points across the waist length 6 mm: these datapoints, that are averaged, are circled in Fig. 7.6 c). The averaged waist radii of eight of our samples are shown in Fig. 7.6 d), with the error bars representing a statistical one standard deviation uncertainty. The optical transmission efficiencies for these eight samples in consecutive order are: 97 %, 85%, 96%, 85%, 98%, 99%, 97%, 97%.

The shaded region in Fig. 7.6 d) corresponds to $\pm 5\%$ deviations from the theoretically predicted

nanofiber waist radius $r_{\mathrm{w}} = 215$ nm, using $L_{\mathrm{w}} = 5.9$ mm, the red line labeled (ii). Fig. 7.6 e) shows the theory and SEM datapoints for one particular sample, and Fig. 7.6 f) shows two of hundreds of SEM images we took in characterizing our fabricated tapered fiber samples. We note that the shaded orange regions in Fig. 7.6 a-b) represent the fiber radius range where it is most critical to ensure a smooth and gradual tapering slope to avoid excitation of a higher order mode, potentially causing optical transmission loss. This is discussed further in Sec. 7.3.4.

7.3.4 Adiabaticity and transmission efficiency

As discussed at the beginning of Sec. 7.3, an important quality of a tapered fiber is its adiabatic shape profile, which minimizes excitation of high order modes at the tapering region, and which will be lost when the taper gets sufficiently small in diameter so as to be unable to support these higher-order modes. To have a high optical transmission efficiency, one needs to ensure that the propagating optical energy stays in the fundamental guided mode as the fiber tapers down from the initial core-cladding waveguide (125 μm cladding diameter), to cladding-air waveguide, to the smallest diameter nanofiber waist (430 nm diameter), and all the way back to the core-cladding waveguide as it tapers up to 125 μm diameter.

The adiabaticity condition can be quantified by an adiabaticity criterion [25, 155] given below, which requires the slope of the taper at a position z along the fiber axis, $\theta(z) = \arctan(|dr/dz|)$ to be small (gentle) relative to the product of the radius $r(z)$ and difference of propagation constants $\Delta\beta = |\beta_1 - \beta_2|$ of the fundamental (β_1) and first higher-order mode (β_2) (which is the closest mode that could be excited and lead to energy loss through the tapered fiber):

$$\theta(z) \ll \frac{r\Delta\beta}{2\pi}, \tag{7.10}$$

where we note that, as derived in [155], the two-mode coupling strength is associated with the beat length between the two modes, $z_{\mathrm{b}} = 2\pi/\Delta\beta$. Refer to Fig. 7.7 a) for illustration of the tapered fiber radius $r = r(z)$, slope $\theta(z)$, at position z along the fiber.

As evident from the form of the adiabaticity criterion given by Eq. (7.10), the critical slope $\theta_{\mathrm{c}} = \frac{r\Delta\beta}{2\pi}$ is determined by the quantity $\Delta\beta$, which is a function of the fiber radius $r(z)$ so that $\Delta\beta = \Delta\beta(r(z))$. Consequently, the adiabaticity criterion is most demanding at the locations z where $\Delta\beta(z)$ is the smallest. Fig. 7.7 c) shows the functions $\beta(r)/k$ for the core-cladding guided modes HE_{11} and HE_{12} labeled 1a (blue) and 1b (black) respectively, and the cladding-air guided modes HE_{11} and HE_{12} labeled 2a (red) and 2b (green) respectively, where $k = 2\pi/\lambda$ and $\lambda =$

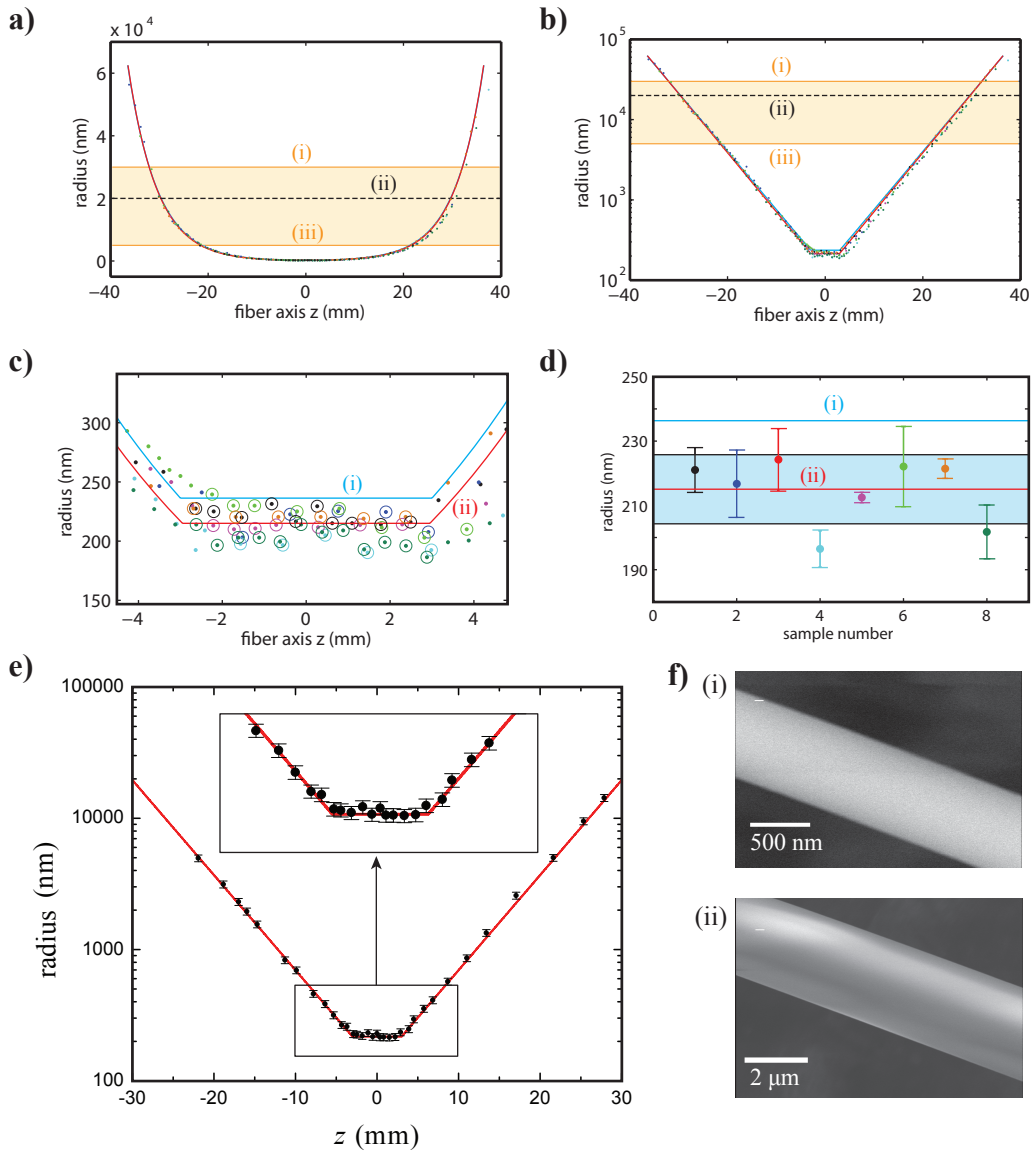

Figure 7.6: **Tapered nanofiber shape. a)** Theoretical prediction (curves) and measurement data points of seven fabricated tapered nanofiber samples, showing the taper radius (r) as a function of position (z) along the fiber axis. The shaded region between (i) and (iii) shows the taper radius range where it is most critical to have a small slope ($\frac{dr}{dz}$) to ensure adiabaticity and high taper transmission efficiency. **b)** The plot in logarithmic scale, showing the exponential decay profile (linear in logarithmic scale) and uniform waist radius at the 6 mm center nanofiber region. **c)** Expanded view around the nanofiber waist, showing theoretical curves for heating length $L_w = 6$ mm (i) and $L_w = 5.9$ mm (ii), and data points where circled data points are averaged and shown as the sample waist radii in d). **e)** Data points and theory curve for one of the seven samples. **f)** Hundreds of SEM images from seven samples like these make up the data points in a-e).

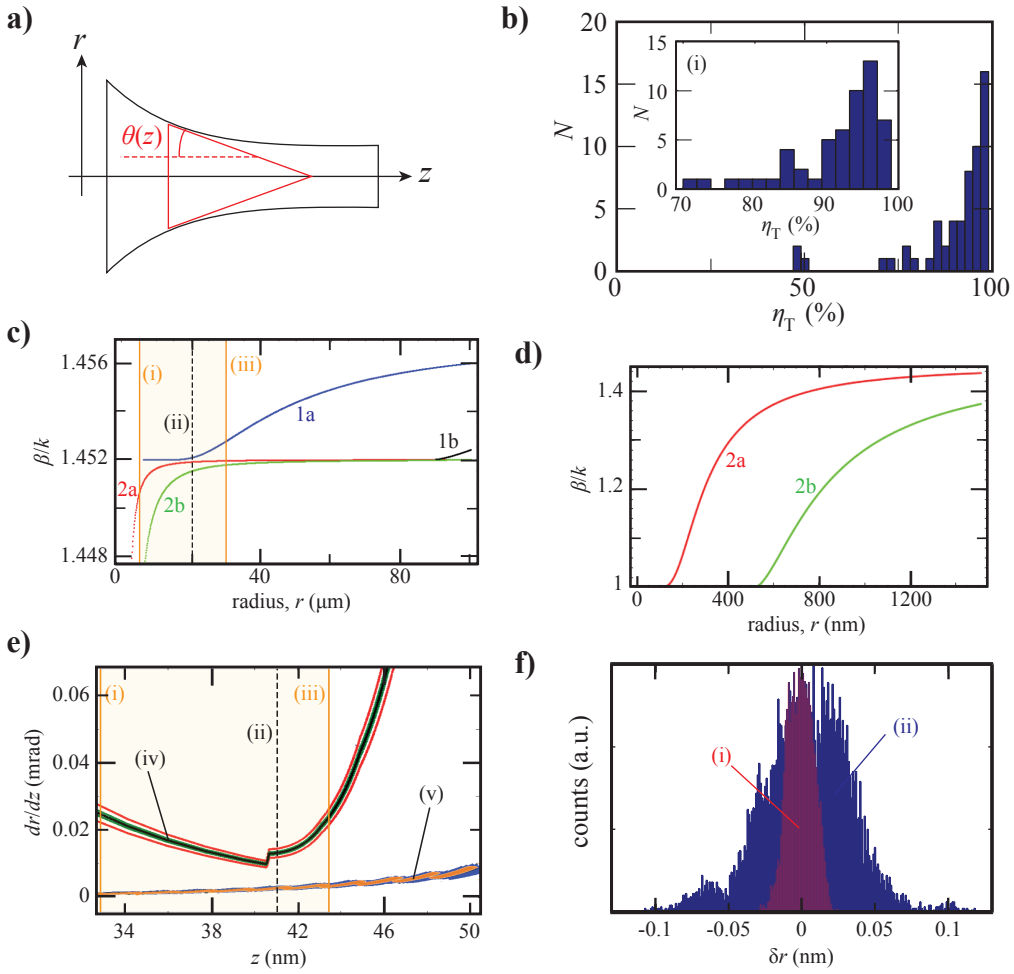

Figure 7.7: **Adiabaticity condition and nanofiber transmission efficiency. a)** Cross-sectional plot showing taper radius (r) along the fiber axis (z) and the local slope $\theta(z) = \arctan(\frac{dr}{dz})$. **b)** Histogram of $N = 57$ total fabricated taper samples, with number of samples $N = 41$ for $T \geq 90\%$, and $N = 26$ for $T \geq 95\%$. **c)** Normalized guided mode propagation constant β/k, $k = 2\pi/\lambda, \lambda = 852$ nm as a function of taper radius (r), for core-cladding modes, HE_{11} (1a, blue) and HE_{12} (1b, black), and cladding-air modes, HE_{11} (2a, red) and HE_{12} (2b, green). The expanded plot for these HE_{11} (2a, red) and HE_{12} (2b, green) modes are shown in d). The dashed line (ii) in c) and e) show the radius where β (for HE_{11} core-cladding mode) is closest to β (for HE_{12} cladding-air mode), where it is most critical to suppress the slope $\frac{dr}{dz}$, to avoid excitation of the higher-order mode HE_{12} that would lead to transmission loss as it will leak out at the small radius region where it is not supported by the waveguide ($r < 0.5$ μm as can be seen in panel d)). The shaded region bounded by (i) and (iii) represents the region close to this critical radius (ii). **e)** Simulation of fiber profile slope $\frac{dr}{dz}$ as a function of z; (top) adiabaticity criterion (black) with $\pm$ 3% taper radius (green) and $\pm$ 10% taper radius (red); (bottom) stochastic simulation of the slope distribution of 100 taper pulling runs, using motorized stages with higher specification (orange) vs lower specification (blue). **f)** Stochastic simulation of 100 taper pulling runs result showing $\pm$ 2% nanofiber waist radius spread for the higher spec stages (i) and $\pm$ 5% radius spread for the lower spec motoroized stages (ii). Details of the motorized stages specifications are discussed in the text.

852 nm. The dashed line labeled (ii) shows the taper radius $r = r_{\mathrm{crit}} \approx 20$ μm where $\Delta\beta(r)$ is smallest. The yellow-shaded region bounded by lines (i) and (iii) shows the region close to this taper radius r_{crit}. This taper radius r_{crit} and the shaded region are also shown in Fig. 7.7 e), and also in Fig. 7.6 a-b), shown throughout as the black dashed line at r_{crit} labeled (ii), with the yellow-shaded region bounded by (i) and (iii). We note that the normalized propagation constants $\beta(r)/k$ for the cladding-air guided modes HE_{11} and HE_{12} are shown in Fig. 7.7 d) labeled 2a (red) and 2b (green) respectively for smaller taper radii.

Fig. 7.7 e) shows a plot of curves, labeled (iv), of the adiabaticity condition $\theta_{\mathrm{c}}(z) = \frac{r\Delta\beta(r(z))}{2\pi}$ for a taper profile similar to the one described in Sec. 7.3.3, near the critical fiber radius r_{crit} as shown by the local minimum of curve (iv). The green and red curves around the black curve (iv) represent $\pm$ 3% and 10% taper radius deviations respectively. We note that the discontinuity near the local minimum of curve (iv) is due to the discontinuity at the transition between core-cladding and cladding-air guided mode solutions which we use in our calculation. The discontinuity should not be present in the full model that takes into account all three core-cladding-air boundary conditions. The main purpose for Fig. 7.7 e) is to compare the slope profile $\theta_{\mathrm{c}}(z)$ to the actual taper slope profile $\theta(z)$ shown by the curve labeled by (v).

The curves (v) are the results of a simulation of the fabrication of 100 tapers, taking into account random noise in the motorized pulling stage's position and velocity, modeled as random variables with normal distributions according to the commercial motorized stage specifications. The size of the fluctuations or randomness is apparent from the thickness of the curves (v), which consists of thousands of numerically simulated datapoints. The blue-colored datapoints correspond to an inferior motorized stage (Newport ILS series), with 4% speed stability and $\pm$ 400 nm position hysteresis/repetability. The orange-colored datapoints correspond to the superior motorized stage (Newport XM series), with 1% speed stability and $\pm$ 100 nm position hysteresis/repeatability. Although this analysis shows that as far as the adiabaticity condition is concerned, neglecting all other factors except for these position and speed stabilities, both types of motors should be sufficiently good. Fig. 7.7 f) shows the distributions of simulated nanofiber waist r_{w} deviations corresponding to the superior and inferior motorized stages, labeled (i) and (ii) respectively. We see that the superior motorized stages lead to $\pm$ 2% variation in the nanofiber waist radius r_{w}, whereas the inferior motorized stages lead to $\pm$ 5% variation. For our fabrication setup, we decided to go with the superior XM series motorized stages, specifically the XML210 and XMS160 models for the bottom (heating) stage and top (pulling) stage respectively.

A histogram showing the distribution of fabricated taper optical transmission efficiencies η_T from a sample of 57 tapers is shown in Fig. 7.7 b). Out of these 57 tapers, 3 tapers have $\eta_T \leq 50\%$, 41 tapers have $\eta_T \geq 90\%$, and 26 tapers have $\eta_T \geq 95\%$. In the figure, N represents the number counts of tapers with the corresponding transmission efficiencies η_T. We note that these efficiencies are measured prior to gluing of the tapers, which on average may reduce the transmission efficiency slightly. In fabricating a tapered fiber for our experiment, typically after less than ≈ 5 consecutive pulls, we were able to find one with quite high efficiency. For example, for the one we used in the experiment discussed in Sec. 7.4 we had an optical transmission efficiency of 98% after tensioning and gluing.

7.3.5 Optical power handling

As discussed at the beginning of Sec. 7.3, it is critical to ensure that there is no dust scatterer on the surface of the nanofiber that could lead to local heating and melting of the fused silica nanofiber by the guided optical power inside vacuum. By performing our fabrication inside a clean-hood as discussed in Sec. 7.3.1, and ensuring careful and clean handling of the tapered nanofibers, including during loading into the vacuum chamber, we have been able to reach quite a high power handling capability with our fabricated nanofibers. Recall that a 'dirty' nanofiber could break with as little as 10 μW of power due to local heating on the nanofiber in vacuum, where heat conductivity and hence dissipation is very limited.

With our setup as described in Sec. 7.3.1, we have fabricated fibers that could guide relatively high amounts of optical power in vacuum without breaking or getting damaged. For the pulling parameters (and hence taper profile) described in Sec. 7.3.3, we tested seven tapered nanofibers inside a vacuum environment, all of which could handle more than 150 mW of optical power (measured at the output of the tapered fiber, after any losses including teflon fiber feedthroughs) without breaking. The highest power that we were able to inject into the nanofiber in this vacuum test setup gives 200 mW measured at the output of the fiber. At this power level, the taper still survives. We were limited by the laser source power so we were not able to test for higher power. In these high power tests, we used a laser wavelength of $\lambda = 852$ nm, using the output from a Ti:Sapph laser, or an optical tapered amplifier seeded by a Ti:Sapph laser.

The presence of the dust scatterers that we have been discussing, in most cases, can be detected by simply looking into the light coming out of the tapered nanofiber. An example of this is shown in Fig. 7.8, where in part a), the nanofiber condition is very clean and good, as can be seen by the

faint glow at the nanofiber region (indicated by the white arrow). In part b), this glowing (that is due to Rayleigh scattering of the fused silica material) glows brighter, but it is still uniformly distributed, suggesting absence of 'large' deadly dust scatterer on the surface. In part c) however, we see one distinct (discrete) local dust scatterer around the center of the nanofiber, which glows very brightly relative to the uniform Rayleigh scattering. In most cases, one single dust scatterer like this is sufficient to break the nanofiber through local heating when the fiber is placed inside a vacuum environment, even at a modest 10-100 μW optical power. If we wait longer, we then see many more of these deadly dust scatterers glowing on the surface of the nanofiber, see Fig. 7.8 d). The photos in parts a-d) were taken over a period of about 30-40 minutes in total, with each photo taken at a ≈ 10 minute interval. Here, the tapered fiber is placed in a box in air, with an air current flowing through the box, on an optical table. Note that this particular setup is not designed to keep the fiber clean, but to illustrate this process of accumulation of scatterers. In other setups near our vacuum chambers, we used HEPA filtered cleanhood fan and formed plastic shields around the setup (see Fig. 7.8 e)), where we could maintain clean air current inside the space. In this case, we conducted a similar test, and found we could keep the tapered fiber in clean condition for multiple days. One of the key factors here is the presence of a clean air current that continually flows through the nanofiber sample, preventing large dust scatterers from sticking.

Figure 7.8 f-j) show SEM images of a tapered fiber that was initially well fabricated with high transmission and ability to handle large amounts of power mounted inside a vacuum chamber and overlaped with magneto-optically trapped cesium clouds. After a period of time, we found that the tapered nanofiber broke without any change in the amount of optical power propagating through it. These photos show SEM images of this broken tapered nanofiber, which had been exposed to cesium atoms. As is apparent, we see (most likely) cesium sticking onto the surface of the nanofibers, in various configurations at different parts of the taper as can be seen from the SEM images.

7.4 Nanofiber trap experiment

In this section we present a summary of our experimental realization of an optical trap that localizes single Cs atoms $\simeq 215$ nm from surface of a dielectric nanofiber as we reported in [91]. Implementing our magic-compensated scheme discussed in Sec. 7.2 by operating at magic wavelengths for pairs of counter-propagating red- and blue-detuned trapping beams, differential scalar light shifts are eliminated, and vector shifts are suppressed.

An overview of our experiment is given in Fig. 7.9. A cloud of cold Cesium atoms (diameter ~ 1

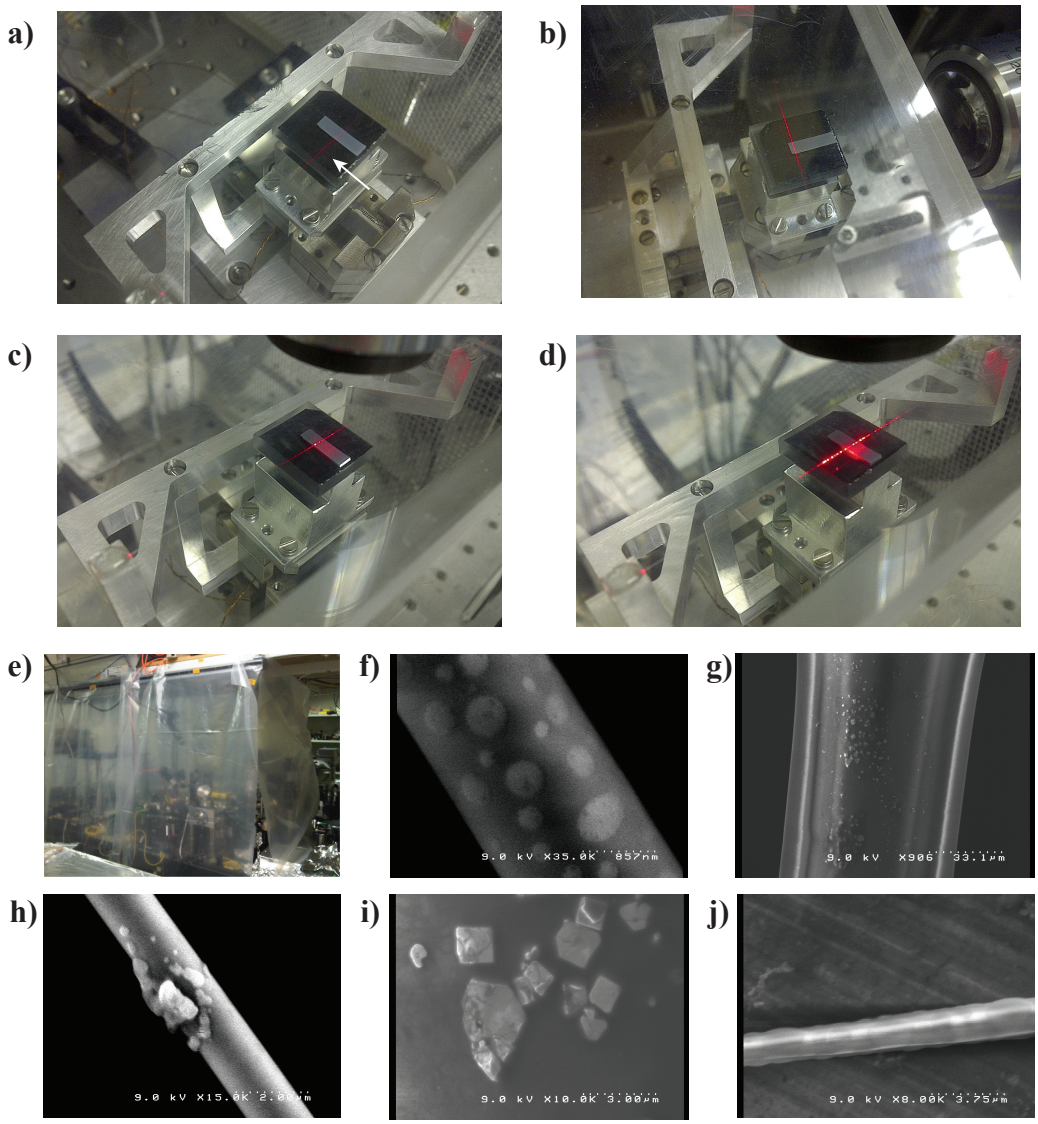

Figure 7.8: **Scatterers and contamination on nanofiber samples. a)** Faint glow visible from a nanofiber in a clean and good condition. **b)** Brighter glow as cleanliness decreases, but the glowing from Rayleigh scattering is still uniformly distributed, suggesting absence of large scatterers. **c)** One large scatterer can be observed, associated with the bright glowing point. One large scatterer such as this could be sufficient to induce local heating and melting with optical guided power of 10-100 μW inside vacuum environment. The setup in the photo here is in air (not in vacuum). **d)** Numerous large scatterers observed. The photos in a-d) were taken over a period of about 30-40 minutes with $\approx$ 10 minutes interval. **e)** Plastic shielded area below a HEPA-filtered cleanhood fans above our experiment setup. Here clean air current could keep a nanofiber sample inside the space clean for multiple days. **f-j)** SEM images of broken (melted by guided optical power) tapered nanofiber which had been exposed to cesium atoms inside a vacuum chamber.

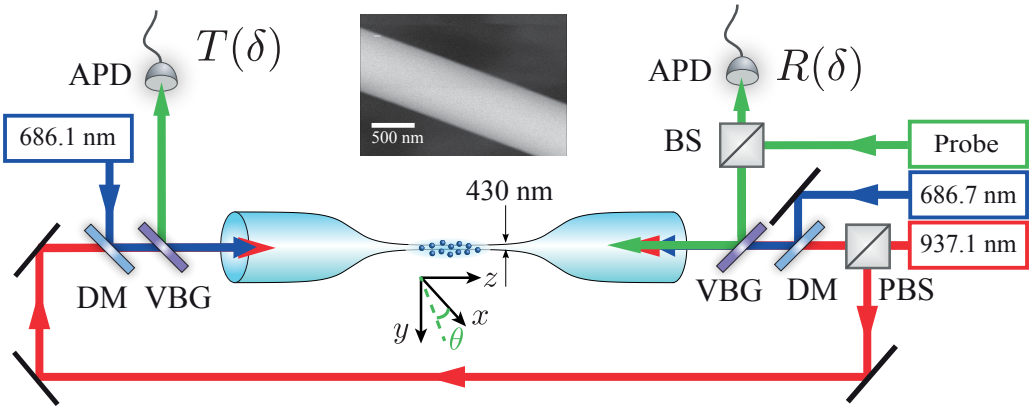

Figure 7.9: **Nanofiber atom trap setup.** Schematic of the setup for a state-insensitive, compensated nanofiber trap. VBG: volume Bragg grating, DM: Dichroic mirror, PBS: polarizing beamsplitter, and APD: avalanche photodetector. The inset shows an SEM image of the nanofiber for atom trapping.

mm) spatially overlaps the nanofiber. Cold atoms are loaded into U_{trap} during an optical molasses phase ($\sim$ 10 ms) and are then optically pumped to $6S_{1/2}, F = 4$ for 0.5 ms. The red- and blue-detuned trapping fields are constantly 'on' throughout the laser cooling and loading processes with parameters as shown in Fig. 7.3. For the transmission and reflection measurements, the trapped atoms are interrogated by a probe pulse (1 ms) with frequency ω_P, optical power $P_{\text{probe}} \simeq 0.1$ pW and detuning $\delta = \omega_P - \omega_A$ relative to the $F = 4 \leftrightarrow F' = 5$ transition frequency ω_A. The probe pulse is combined with the forward propagating trapping fields by a pair of volume Bragg gratings (VBGs) at the fiber input. The strong trapping beams are then filtered by a pair of VBGs at the fiber output, with the transmitted probe pulse monitored by a single-photon avalanche photodiode. The polarization of the probe laser is aligned along the trapping beams in order to maximize the overlap with the trapped atoms. We then shelve the atoms to $F = 3$ with a depumping pulse, and probe the fiber transmission with a reference pulse to determine the input power of the probe pulse.

Utilizing our magic-compensation scheme, we realized trapping of up to 825 cesium atoms along a one-dimensional array of length $L \approx 1$ mm, using our fabricated SiO_2 nanofiber of diameter 430 nm (Sec. 7.3). The lifetime for atoms in our nanofiber trap is determined from the decay of the resonant optical depth $d_N \simeq N\sigma_0/A_{\text{eff}}$ as a function of storage time τ, measured by the absorption of a probe light transmitted along the fiber, through the 1-D array of trapped atoms. Here, N is the number of trapped atoms, $\sigma_0 = \lambda^2/(2\pi)$ is the resonant absorption cross-section, and $A_{\text{eff}} = P_{\text{probe}}/I_{\text{probe}}(\vec{r}_{\text{min}})$ is the effective optical mode area of the probe's evanescent wave. We observe that d_N decays exponentially with time constant $\tau_0 = 12 \pm 1$ ms. With pulsed polarization-gradient cooling, the lifetime is extended to $\tau_{\text{PG}} = 140 \pm 11$ ms. We measured a maximum resonant

optical depth $d_N = 66 \pm 17$ at $\tau = 1$ ms (with 825 atoms trapped along a 1-D array next to our nanofiber). Our magic-compensated scheme leads to a state-insensitive (non-intrusive) trapping with no discernible shift of the transition frequency $\Delta_A/2\pi \simeq 0 \pm 0.5$ MHz relative to the free-space line center. We measured a linewidth of our trapped atoms of $\Gamma/2\pi \simeq 5.7 \pm 0.1$ MHz, as compared to the free-space radiative linewidth $\Gamma_0/2\pi = 5.2$ MHz for the $6S_{1/2} \leftrightarrow 6P_{3/2}$ transition. By contrast, for a non-compensated scheme without magic wavelengths for Cs [248], the transition frequency is shifted by $\Delta_A/2\pi \simeq 13$ MHz and the linewidth is broadened to $\Gamma/2\pi \simeq 20$ MHz.

We estimate the number of trapped atoms by knowledge of single-atom attenuation (optical-depth), $d_1 = d_N/N \simeq 0.08$, where N is the number of trapped atoms, and d_N is the total optical depth due to absorption by N trapped atoms. The single-atom attenuation d_1 is infered from the saturation measurement where we monitor the total absorption d_N as a function of the probe power P. Specifically, the number of trapped atoms can be determined (using a generalized Beer's law [248, 91]) by measuring the total absorbed power $P_{\rm abs}$ absorbed by the trapped atomic ensemble in the limit of high saturation $s = P/P_{\rm sat} \gg 1$, where $P_{\rm sat} = I_{\rm sat} A_{\rm eff} = 49.6$ pW, effective optical mode area is $A_{\rm eff} = 1.8\ \mu{\rm m}^2$ (for our nanofiber), σ_0 is the resonant absorption cross-section, and $n_z = N/L$ is the atomic line density for a sample length $L = 1$ mm. Our saturation measurement was performed at a storage time $\tau = 1$ ms with $\delta = 0$ MHz, yielding a number of trapped atoms of $N = 224 \pm 10$. Here, with the total optical depth $d_N = 18$ in this saturation measurement, we estimate an optical depth per atom $d_1 = (7.8 \pm 1.3) \times 10^{-2}$.

The measurement results of our nanofiber trap experiment can be found in our paper [91]. In addition to the abovementioned results, we have also observed reflections of a probe light by the trapped atoms, where weak but detectable reflection signals were measured. We observed increase in the linewidth of the reflection spectral signal with increasing number of trapped atoms N, in direct proportion to the entropy for the multiplicity of trapping sites.

7.5 Summary

In conclusion, in this chapter we have discussed our proposed magic-compensated scheme for a state-insensitive optical nanofiber trap in Sec. 7.2, the fabrication of a tapered optical nanofiber with qualities required to realize such a nanofiber trap in Sec. 7.3, and the experimental demonstration of such a state-insensitive nanofiber trap in Sec. 7.4.

We discussed a specific example of our state-insensitive nanofiber trap scheme that provides three-dimensional confinement of cesium atoms in close proximity to a nanofiber. The trap is formed by a

pair of counter-propagating red-detuned beams ($\lambda_{\rm red} = 937.1$ nm with power $P_{\rm red} = 2\times$ 0.4 mW) and a pair of counter-propagating blue-detuned beams ($\lambda_{\rm blue} = 686.1$ nm with power $P_{\rm blue} = 2\times$ 5 mW, with relative detuning of 382 GHz). With scalar shift cancellation and a vector shift suppression by more than a factor of 250, a trapping potential is formed at 215 nm away in the radial direction from the surface of the 430 nm diameter nanofiber, with radial, axial and azimuthal trap frequencies $\{\nu_\rho, \nu_z, \nu_\phi\}/2\pi = \{199, 273, 35\}$ kHz respectively.

Note that there were errors in our initial calculation in [142], which led to the magic wavelength values $\lambda_{\rm red} = 937.1$ nm and $\lambda_{\rm blue} = 686.1$ nm, which were the wavelengths used in our experiment. Correction to our calculation [64] later led to the correct magic wavelength values $\lambda_{\rm red} = 935.3$ nm and $\lambda_{\rm blue} = 684.9$ nm. The calculation for the trap potential for our experiment (Fig. 7.3) is based on the corrected equations [64], for the actual wavelengths used in the experiment, which were $\lambda_{\rm red}$ = 937.1 nm and $\lambda_{\rm blue} = 686.1$ nm.

Following our discussion of the state-insensitive magic-compensated scheme, we discussed our fabrication of a tapered optical nanofiber, with qualities including relatively small nanofiber waist diameter, high repeatability and predictability of nanofiber shape profile, high optical transmission efficiency, and large power-handling capability for a nanofiber inside a vacuum environment. We characterized more than 50 tapered nanofiber samples fabricated using our optimized fabrication setup and parameters, where we achieve a transmission efficiency of $\eta_T > 95\%$ for one in every two fiber pulls. The tapered fibers have waist radii of $r_{\rm w} = 215 \pm 10$ nm, and they have been tested to be able to handle guided optical power in excess of 200 mW in vacuum (measured at the output of the fiber) without breaking. The fully computer-controlled fabrication process provides good yield and repeatability, and good agreement (within $\pm 5\%$) between predicted and actual tapered fiber shape profile.

In this third part of this chapter, we present a summary of our experimental realization of a state-insensitive nanofiber trap using our magic-compensated scheme and fabricated nanofiber, where we trapped up to 825 atoms leading to an atom-resonant fiber-guided light transmission of $T \simeq \exp(-66)$ (i.e., an optical depth of 66), with a single atom absorption of about 8% ($T_1 \simeq \exp(-0.08) = 0.92$, a single atom resonant optical depth of 0.08). We observed the effectiveness of our magic-compensated schemes leading to the elimination of scalar shifts and suppression of vector shifts by a factor of ≈ 250. Our absorption spectroscopy measurement shows negligible shift of the atomic resonant frequency relative to the free-space value $\Delta_A/2\pi \simeq 0 \pm 0.5$ MHz, with a linewidth of $\Gamma/2\pi \simeq 5.7 \pm$ 0.1 MHz, which is slightly larger than the free-space linewidth of $\Gamma_0/2\pi = 5.2$ MHz, something

we attribute to the enhanced atomic scattering rate into the fiber guided mode, presence of tensor shifts, Casimir-Polder shifts, and technical noise of our probe laser.

Compared to previous work with hollow-core and nano-fibers, the atoms are trapped with small perturbations to dipole-allowed transitions. Our scheme is thus well-suited to various applications, including the creation of 1D atomic mirrors for cavity QED and investigations of single-photon nonlinearities and quantum many-body physics in 1D spin chains [41], as well as precision measurements of Casimir-Polder forces near a dielectric waveguide [176]. Currently, the maximum filling factor for sites over the 1 mm loading region is $\sim 19\%$, which can be improved with adiabatic loading and elimination of collisional blockade [96]. The vibrational ground state for axial motion in U_{trap} can be reached by introducing Raman sidebands on the 937 nm trapping fields [30]. The strong axial confinement in our trap implies the presence of a large anharmonicity in the vibrational ladder, which could provide a tool for experiments with single phonons. Furthermore, the design principles of our magic, compensated trap can be extended from simple 'nanowires' to hybrid systems such as nanofiber-microtoroidal cavity systems as discussed in Chapter 6, as well as photonic crystal structures [73] as discussed in Chapters 3 and 8.